

# Fractal-IR: A Unified Framework for Efficient and Scalable Image Restoration

Yawei Li<sup>1</sup> Bin Ren<sup>2,3</sup> Jingyun Liang<sup>1</sup> Rakesh Ranjan<sup>4</sup> Mengyuan Liu<sup>5</sup>  
 Nicu Sebe<sup>3</sup> Ming-Hsuan Yang<sup>6</sup> Luca Benini<sup>1</sup>  
<sup>1</sup>ETH Zürich, <sup>2</sup>University of Pisa, <sup>3</sup>University of Trento, <sup>4</sup>Meta Reality Labs,  
<sup>5</sup>Peking University, <sup>6</sup>University of California, Merced

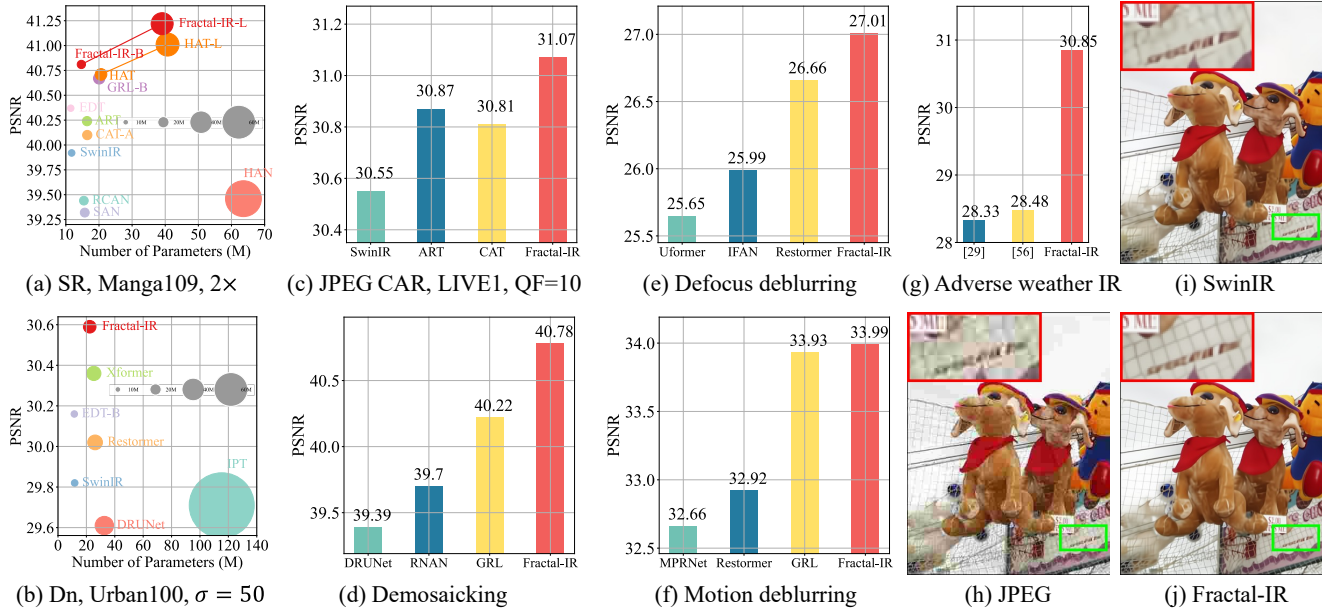


Figure 1. The proposed *Fractal-IR* is notable for its efficiency and effectiveness (a)-(b), generalizability across seven image restoration tasks (a)-(g), and improvements in the visual quality of restored images (h)-(j).

## Abstract

While vision transformers achieve significant breakthroughs in various image restoration (IR) tasks, it is still challenging to efficiently scale them across multiple types of degradations and resolutions. In this paper, we propose *Fractal-IR*, a fractal-based design that progressively refines degraded images by repeatedly expanding local information into broader regions. This fractal architecture naturally captures local details at early stages and seamlessly transitions toward global context in deeper fractal stages, removing the need for computationally heavy long-range self-attention mechanisms. Moreover, we observe the challenge in scaling up vision transformers for IR tasks. Through a series of analyses, we identify a holistic set of strategies to effectively guide model scaling. Extensive experimental results show that *Fractal-IR* achieves state-of-the-art performance in seven common image restoration tasks, including super-resolution, denoising, JPEG artifact removal, IR in adverse weather conditions, motion deblurring, defocus deblurring, and demosaicking. For  $2\times$  SR on *Manga109*,

*Fractal-IR* achieves a 0.21 dB PSNR gain. For grayscale image denoising on *Urban100*, *Fractal-IR* surpasses the previous method by 0.2 dB for  $\sigma = 50$ .

## 1. Introduction

Image restoration (IR) aims to improve image quality by recovering high-quality visuals from observations degraded by noise, blur, and downsampling. To address these inherently ill-posed problems, numerous methods have been developed primarily for a single degradation, including convolutional neural networks (CNNs) [20, 53], vision transformers (ViTs) [9, 52], and state space models (Mamba) [28].

Despite the advancements, a key challenge remains: *how to design a model that can efficiently handle multiple IR tasks and scale up to accommodate various image resolutions and degradation complexities*. Recent transformer-based solutions have focused on improving the efficiency of self-attention, often by partitioning images into smaller windows and refining local details. Yet, such design risk

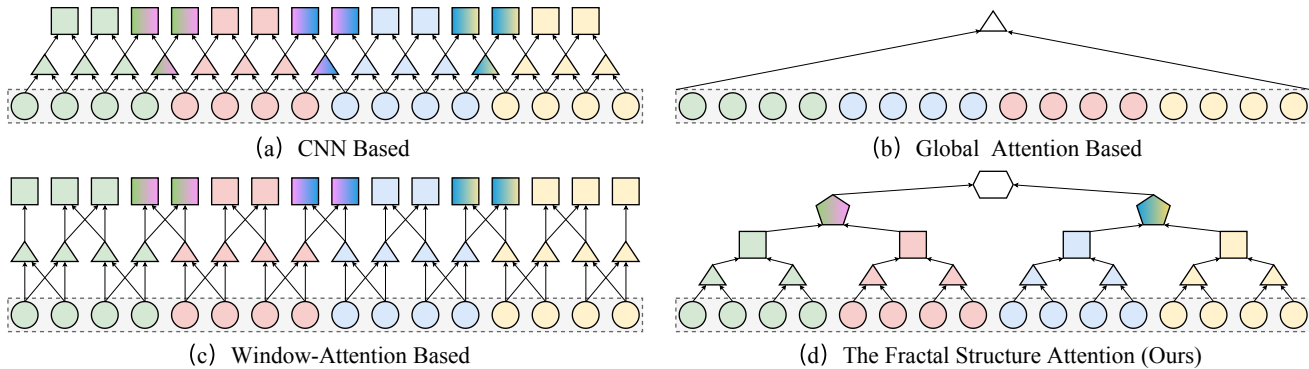


Figure 2. Illustration of information flow principles. The colors represent local information, with their blending indicating propagation beyond the local region. (a) The CNN-based. (b) The global attention based. (c) Window attention based. (d) The proposed hierarchical information flow prototype.

isolating spatial regions and may require additional operations (*e.g.*, window shifting) [16, 52] or large receptive fields to capture global context [11, 48]. As image resolutions grow and degradations vary, purely local or fully global mechanisms can become either insufficiently expressive or computationally prohibitive.

To address the efficiency issue, we propose a fractal-based framework shown in Fig. 2(d) for IR. In our approach, local details are initially processed in smaller fractal cells, then repeatedly expanded and merged, mirroring how fractals capture both micro-level patterns and macro-level structures [6, 40, 46]. Each fractal iteration fuses information from earlier stages, ensuring that local details and broad contexts reinforce one another without incurring the high computational costs of naive global self-attention.

Despite the advantages of the fractal design, scaling the model beyond 50M parameters still remains challenging, as evidenced by the degraded performance of larger models [11, 53]. Further investigation attributes this issue to several factors including parameter initialization, training strategy, and operator design. To address these challenges, we propose a holistic set of three strategies for effective model scaling, including replacing heavyweight convolutions with more efficient alternatives, implementing a warm-up phase during training, and using dot-product self-attention. These strategies enable the successful training of larger IR models.

The proposed *Fractal-IR* framework has the advantages of efficiency, scalability, and generalization for IR tasks. 1) By progressively expanding compact representations through fractal stages, *Fractal-IR* captures broader structures and semantics without resorting to dense, full-image attention. This leads to notably lower memory usage and computational overhead compared to standard transformer-based approaches. 2) The fractal design inherently supports deeper or wider expansions, enabling the model to scale effectively while maintaining efficiency. With the proposed model scaling strategies, *Fractal-IR* can be successfully scaled up to provide large capacity and capture

richer patterns. 3) Empirical results show that the proposed *Fractal-IR* framework generalizes well across different IR tasks, consistently achieving strong performance across different types of degradation and restoration challenges.

Our main contributions are summarized as follows:

- We introduce a novel fractal-based design for image restoration, which facilitates progressive global information exchange and mitigates the curse of dimensionality.
- We examine the challenge of training convergence for model scaling-up in IR and propose mitigation strategies.
- Extensive experiments validate the effectiveness of the proposed method. *Fractal-IR* consistently outperforms state-of-the-art IR methods for multiple tasks.

## 2. Related Work

**Image Restoration.** The focus of IR is to recover high-quality images from their degraded counterparts. As a challenging problem, IR has captured substantial interest, leading to practical applications such as denoising [8, 17, 27, 97], deblurring [43, 68, 74], super-resolution (SR) [22, 69, 91], demosaicking [61, 101], JPEG compression artifacts removal [12], *etc.* The landscape of IR has shifted with the evolution of deep learning and the increased availability of computational resources. Many CNN models have been proposed [4, 20, 51, 97] for different IR tasks. However, despite their effectiveness, CNNs have been found to struggle in propagating long-range information within degraded input images. This challenge is attributed to the limited receptive field of CNNs, which constrains the overall performance of CNN-based methods [13, 48, 95]. Thus, transformer-based models are proposed to solve this problem [9, 52, 93]. Yet, the computational complexity of transformers scales quadratically with the number of tokens. To solve this problem, recent methods utilize state-space models which have linear complexity growth [26, 28].

**Hierarchical Models.** Modeling image hierarchies is essential for IR tasks. Traditional CNNs progressively prop-

agate information to the global range with stacked convolutional layers. However, this has not been efficient. Thus, non-local operators were proposed [54, 55, 65, 104] to enhance the global modeling capacity of CNNs. With the advent of transformers [9, 21, 85], image hierarchies are modeled via a combination of self-attention and convolution operations. Various methods have been proposed to achieve efficient and effective self-attention for hierarchical image modeling. SwinIR [52] conducts multi-head self-attention (MSA) window-wise. A shift operation is applied to enable information exchange between windows [57]. Uformer [88] and Restormer [93] proposes to propagate information hierarchically with a UNet structure but still with window self-attention. Other methods refine self-attention with much more exquisite efforts, including rectangle-window self-attention [47], sparse self-attention [31], and graph-attention [72], spatial shuffle [31], and random spatial shuffle [89]. More recently, fractal structures are utilized for image generation [46], which offers a significant improvement of generation efficiency. In this paper, we propose a general and efficient IR solution which hierarchically propagates information within a fractal architecture.

### 3. Methodology

#### 3.1. Motivation

Table 1. Removing shifted windows leads to degraded SR performance. PSNR is reported on Urban100 dataset for 4× SR.

Training Dataset	Window Shift	
	No	Yes
DF2K [3]	27.45	27.18(-0.27)
LSDIR [49]	27.87	27.64(-0.23)

Table 2. Plateau effect of enlarged window size reported for 4× SR. Window size larger than 32 is not investigated due to OOM.

Test set	Window size	PSNR	PSNR gain	GPU Mem.	Computation
Urban100	8	27.42	0.00	14.63GB	1×
	16	27.80	0.38	17.22GB	4×
	32	28.03	0.22	27.80GB	16×

This paper aims to propose an efficient and scalable framework for generalized IR. Before presenting technical details, we discuss the motivation behind the fractal design. **Limitation of Localized Computation.** IR transformers typically conduct localized computation through self-attention in manually partitioned windows, combined with a window shift mechanism [11, 48, 52]. When the flow of contextual information between different regions or features within an image is restricted, a model’s ability to reconstruct high-quality images from low-quality counterparts is significantly hindered. This effect can be observed by isolating the information flow through disabling window shifts in Swin Transformer [52, 57, 58]. As shown in Tab. 1, removing the window shift mechanism leads to a significant PSNR

drop of 0.27 dB for DF2K training and 0.23 dB for LSDIR training. The obvious reductions indicate that information isolation degrades the performance of IR models and suggests that algorithms that effectively leverage broader contextual information can yield superior IR results.

**Saturation in Computation Scaling.** On the other hand, we observe that self-attention computation on fully connected graphs is not always necessary or beneficial for improving the performance of IR networks [9, 93]. As ViTs generate distinct graphs for each token, early attempts to facilitate global information dissemination led to the curse of dimensionality, causing quadratically increasing computational complexity with tokens [57, 86]. Subsequent attention mechanisms, building graphs based on windows, achieve better IR results. However, the benefits of expanding the window size tend to plateau. As shown in Tab. 2, the PSNR of the SR images improves as the window size grows from 8 to 32. Yet, with larger windows, the gains decrease, accompanied by a sharp increase in memory footprint and computational demands. This urges a reassessment of the information propagation mechanism on large windows.

**Effective Fractal Design.** The above analysis emphasizes the crucial role of effective information flow in modern architectural designs. CNN-based methods propagate information slowly within a small region covered by the filter (Fig. 2(a)). A large receptive field has to be achieved by the stack of deep layers. Global attention based ViT propagates information directly across the whole sequence with a single step. However, the computational complexity grows quadratically with the increase of tokens (Fig. 2(b)). To address this problem, window attention in Fig. 2(c) propagates information across two levels but still has a limited receptive field even with shift operation.

To facilitate fast and efficient image modelling, we propose a hierarchical design with the fractal architecture shown in Fig. 2(d). In this model, information flows progressively from the local scope, aggregated in several intermediate levels, and disseminated across the whole sequence. This new fractal design principle is more efficient in that it enables a global understanding of the input sequence with several operations. The actual implementation of the fractal can be configured to ensure computational efficiency. One realization in this work is a three-level structure in Fig. 3. The space and time complexity in Appx. 2 shows that the proposed fractal design is more efficient in propagating information to the global range under similar space and time complexity of window attention.

#### 3.2. Fractal Image Restoration

The fractal computation mechanism consists of three levels and aims to model both the local and the global information for a given feature  $X \in \mathbb{R}^{H \times W \times C}$  efficiently. We denote the information within  $X$  as  $\mathcal{L}_0$  level meta-information.

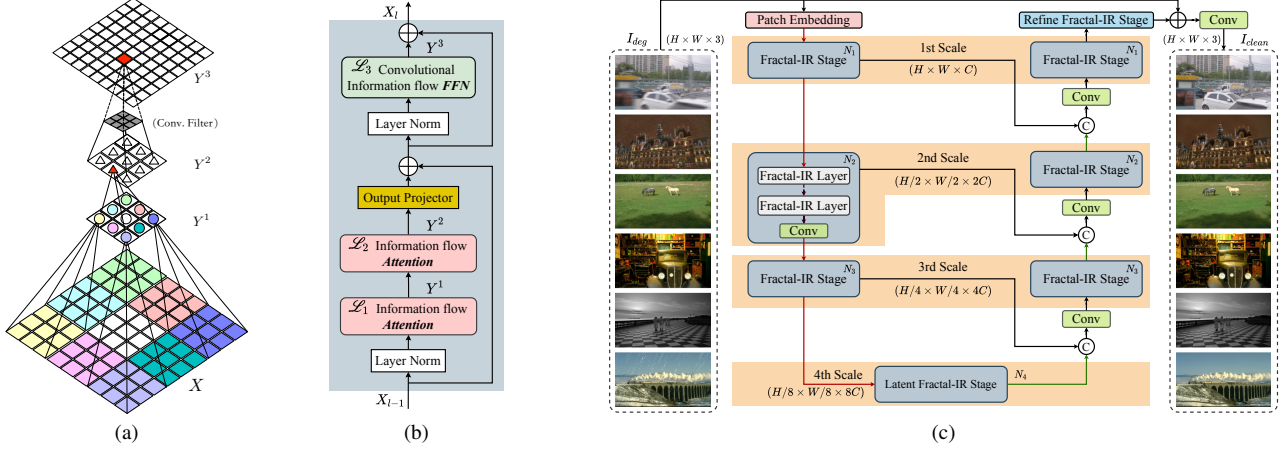


Figure 3. Illustrations of: (a) The proposed fractal information flow. (b) The fractal transformer layer. (c) And the *Fractal-IR* architecture.

**$\mathcal{L}_1$  Local Fractal Layer.** In the beginning of the network, computation is first done in fractal cells by applying MSA to the input feature  $X$  within a  $p \times p$  patch. To facilitate the MSA, the input feature is first partitioned into local patches, leading to  $X' \in \mathbb{R}^{\frac{HW}{p^2} \times p^2 \times C}$ . Then feature  $X'$  is linearly projected into query ( $Q^1$ ), key ( $K^1$ ), and value ( $V^1$ ). Self-attention within the local patches is denoted as

$$Y_i^1 = \text{SoftMax} \left( \frac{Q_i^1 (K_i^1)^\top}{\sqrt{d}} \right) V_i^1, \quad (1)$$

where  $i$  index the windows, and  $d$  is the head dimension. This process is shown in Fig. 3(a). Each node within the  $Y^1$  grid collects the  $\mathcal{L}_0$  level meta-information from its corresponding original window, marked by the same color.

**$\mathcal{L}_2$  Non-Local Fractal Aggregation Layer.** Upon completion of the computation in the local fractal cells, information must be progressively propagated to higher fractal levels. As indicated conceptually in Fig. 2(d), the fractal design requires that information to be progressively aggregated beyond local patches while avoiding direct extension to the global scale. This design is different from the previous operations [31, 89] and is driven by two key considerations: 1) *The computational complexity of attention in the global image can be quite high*; 2) *Not all global image information is relevant to the reconstruction of a specific pixel*. Thus, guided by this design principal, 2D  $s \times s$  non-overlapping local patches  $p \times p$  in  $\mathcal{L}_1$  layer should be grouped together to form a broader  $P \times P$  region for  $\mathcal{L}_2$  layer. Then the dispersed pixels need to be grouped together. The seemingly complex operation is simplified by a reshaping operation and a permutation operation, *i.e.*,

$$\hat{Y} \in \mathbb{R}^{\frac{H}{P} \times s \times p \times \frac{W}{P} \times s \times p \times C} = \text{Reshape}(Y^1), \quad (2)$$

$$Y' \in \mathbb{R}^{(\frac{H}{P} \times \frac{W}{P} \times p^2) \times s^2 \times C} = \text{Permute}(\hat{Y}). \quad (3)$$

The simple permutation operation facilitates the distribution of  $\mathcal{L}_1$  information nodes across a higher  $\mathcal{L}_2$  level.

To better integrate the permuted information  $Y'$ , we further project  $Y'$  to  $Q^2$ ,  $K^2$ , and  $V^2$  and conduct another self-attention to get  $Y^2$ . As a result, the larger patch-wise global information denoted as colorful nodes in  $Y^1$  of Fig. 3 now is well propagated to each triangle node in  $Y^2$  of Fig. 3.

**$\mathcal{L}_3$  Global Modelling Layer.** Finally, non-local information in the broader  $\mathcal{L}_3$  region needs to be aggregated to form a global understanding of the image. To comply with previous designs of transformers, this is achieved by inserting convolutions into the feed-forward network (FFN) of transformers. This layer leads to the final representation  $Y^3$ . As a result, this design not only aggregates all the channel-wise information more efficiently but also enriches the inductive modeling ability [15, 90] for the proposed mechanism.

### 3.3. Fractal-IR Layer

The *Fractal-IR* layer is constructed based on the fractal information flow mechanism (FIFM). The detailed structure shown in Fig. 3(b) serves as the basic component of the proposed IR network. For each *Fractal-IR* layer, the input feature  $X_{l-1}$  first passes through a layer normalization and two consecutive information propagation attentions. After adding the shortcut, the output  $X'_l$  is fed into the convolutional FFN with another shortcut connection and outputs  $X_l$ . We formulate this process as follows:

$$\begin{aligned} X'_l &= \text{FIFM}_{\text{Att}}(\text{LN}(X_{l-1})) + X_{l-1}, \\ X_l &= \text{FIFM}_{\text{Conv}}(\text{LN}(X'_l)) + X'_l, \end{aligned} \quad (4)$$

where  $\text{FIFM}_{\text{Att}}$  consists of both the  $\mathcal{L}_1$  and  $\mathcal{L}_2$  hierarchies, and  $\text{FIFM}_{\text{Conv}}$  denotes the  $\mathcal{L}_3$  module.

### 3.4. Overall architecture

To comprehensively validate the effectiveness of the proposed method, similar to prior methods [10, 48, 72], we choose two commonly used basic architectures including the U-shape hierarchical architecture shown in Fig. 3(c)

and the columnar architecture shown in Appx 1.1. The columnar architecture is used for image SR while the U-shape architecture is used for other IR tasks. Specifically, the degraded low-quality image  $I_{low} \in \mathbb{R}^{H \times W \times 1/3}$  (1 for the grayscale image and 3 for the color image) is first sent to the convolutional feature extractor and outputs the shallow feature  $F_{in} \in \mathbb{R}^{H \times W \times C}$  for the following *Fractal-IR* stages/layers. For the U-shape architecture,  $F_{in}$  undergoes representation learning within the U-shape structure. In contrast, for the columnar architecture,  $F_{in}$  traverses through  $N$  consecutive *Fractal-IR* stages. Both architectures ultimately generate a restored high-quality image  $I_{high}$  through their respective image reconstructions.

#### 4. Scaling Up *Fractal-IR*

Existing IR models are limited to a model size of 10-20M parameters. In this paper, we develop models of medium and large sizes. However, scaling up the model leads to a performance drop as shown in the pink rows of Tab. 3.

Table 3. Model scaling-up exploration with SR.

Scale	Model Size	Warm up	Conv Type	PSNR				
				Set5	Set14	BSD100	Urban100	Manga109
2×	15.69	No	conv1	38.52	34.47	32.56	34.17	39.77
2×	57.60	No	conv1	38.33	34.17	32.46	33.60	39.37
2×	57.60	Yes	conv1	38.41	34.33	32.50	33.80	39.51
2×	54.23	Yes	linear	38.56	34.59	32.58	34.32	39.87
2×	55.73	Yes	conv3	38.65	34.48	32.58	34.33	40.12

Table 4. Investigated weight initialization and rescaling method for model scaling-up. Results reported for SR on Set5.

Method	Description	2×	3×
Zero LayerNorm	Initialize the weight and bias of LayerNorm as 0 [58].	38.35	34.81
Residual rescale	Rescale the residual blocks by a factor of 0.01 [11, 53].	38.31	34.79
Weight rescale	Rescale the weights in residual blocks by 0.1 [87].	38.36	34.84
trunc_normal	Truncated normal distribution	38.33	34.71

Table 5. Comparison of SR results between dot production attention and cosine similarity attention for scaled-up models.

Scale	Attn. type	Set5	Set14	BSD100	Urban100	Manga109
2×	cosine sim	38.43	34.65	32.56	34.13	39.69
2×	dot prod	38.56	34.79	32.63	34.49	39.89
4×	cosine sim	33.08	29.15	27.96	27.90	31.40
4×	dot prod	33.14	29.09	27.98	27.96	31.44

**Initial attempts.** Existing methods handle this problem with weight initialization and rescaling techniques. Chen et al. [11] and Lim et al. [53] reduce the influence of residual convolutional blocks by scaling those branches with a small factor (0.01). Wang et al. [87] rescale the weight parameters in the residual blocks by 0.1. [58] initialize the weight and bias of LayerNorm as 0. In addition, we also tried the truncated normal distribution to initialize the weight parameters. However, as shown in Tab. 4, none of the four methods improves the convergence of the scaled models, indicating that they do work for the IR transformers.

**The proposed model scaling-up solution.** The initial investigation indicates that the problem can be attributed to

the training strategy, the initialization of the weight, and the model design. Thus, three methods are proposed to mitigate the model scaling problem. *First*, we warm up the training for 50k iterations at the beginning. As shown in Tab. 3, this mitigates the problem of degraded performance of scaled up models, but does not solve it completely. *Secondly*, we additionally replace heavyweight  $3 \times 3$  convolution (conv1 in Tab. 3) with lightweight operations besides warming up the training. Two alternatives are considered including a linear layer (linear in Tab. 3) and a bottleneck block with 3 lightweight convolutions ( $1 \times 1$  conv+ $3 \times 3$  conv+ $1 \times 1$  conv, conv3 in Tab. 3). Tab. 3 shows that removing the large  $3 \times 3$  convolutions leads to a much better convergence point for the large models. Since the bottleneck block leads to better PSNR than linear layers in most cases, it is used in the other experiments. *Thirdly*, we investigate the influence of dot product attention [57] and cosine similarity attention [58] on the convergence of the large models. Tab. 5 shows that dot product self-attention performs better than cosine similarity self-attention. Thus, dot product self-attention is used throughout this paper unless otherwise stated.

**Why does replacing heavyweight convolution work?** We hypothesize that this strategy works because of the initialization and backpropagation of the network. In Xavier and Kaiming weight initialization, the magnitude of the weights is inversely related to  $f_{in} / f_{out}$  of a layer, *i.e.*,

$$f_{in} = c_{in} \times k^2, \quad (5)$$

$$f_{out} = c_{out} \times k^2, \quad (6)$$

where  $f_{in}$  and  $f_{out}$  denotes  $f_{in}$  and  $f_{out}$ ,  $c_{in}$  and  $c_{out}$  denotes input and output channels, and  $k$  is kernel size. When a dense  $3 \times 3$  convolution is used,  $f_{in}$  and  $f_{out}$  can be large, which leads to small initialized weight parameters. This in turn leads to small gradients during the backpropagation. When the network gets deeper, the vanishing gradients could lead to slow convergence. When dense  $3 \times 3$  convolution is replaced by linear layers or bottleneck blocks, either the kernel size or the number of channels is reduced. Thus, both the two measures decreases the  $f_{in}$  and  $f_{out}$ , leading to larger initialized weights.

**Why does warmup work?** Warmup is effective for training large models primarily because it mitigates issues related to unstable gradients and helps the optimizer gradually adapt to the model’s large parameter space [25, 33]. In the early stages of training, the model’s parameters are initialized randomly. A high learning rate at this stage can cause large updates, leading to unstable or divergent training due to exploding or vanishing gradients. Warmup starts with a small learning rate and gradually increases it, allowing the optimizer to find a stable path in the loss landscape before applying larger updates.

**Why does dot product work better?** We analyze the gradient of dot product and cosine similarity as follows. Sup-

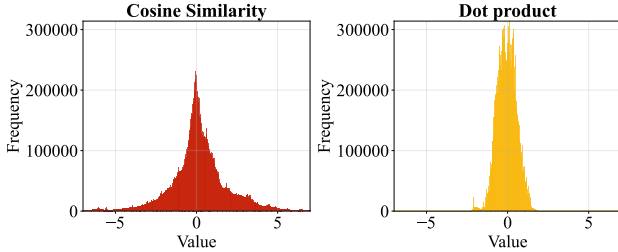


Figure 4. Gradients of cosine similarity and dot product attention.

pose  $\mathbf{q}$  denotes the query and  $\mathbf{k}$  denotes the keys. Then dot product and cosine similarity between  $\mathbf{q}$  and  $\mathbf{k}$  are denoted as  $\text{dot\_prod}(\mathbf{q}, \mathbf{k})$  and  $\text{cos\_sim}(\mathbf{q}, \mathbf{k})$ . The gradient of dot product and cosine similarity with respect to  $\mathbf{q}$  are

$$\frac{\partial}{\partial \mathbf{q}} \text{dot\_prod}(\mathbf{q}, \mathbf{k}) = \mathbf{k}, \quad (7)$$

$$\frac{\partial}{\partial \mathbf{q}} \text{cos\_sim}(\mathbf{q}, \mathbf{k}) = \frac{1}{\|\mathbf{q}\|} \left( \hat{\mathbf{k}} - \text{cos\_sim}(\mathbf{q}, \mathbf{k}) \hat{\mathbf{q}} \right), \quad (8)$$

where  $\hat{\mathbf{q}}$  and  $\hat{\mathbf{k}}$  are normalized  $\mathbf{q}$  and  $\mathbf{k}$ . The gradients with respect to  $\mathbf{k}$  have the similar form. The gradient of cosine similarity involves more terms compared to the gradient of the dot product. This increased complexity in the gradient of cosine similarity makes it more prone to producing large or even unstable gradient values. We conducted a numerical analysis of the gradient values for the two attention methods. As shown in Fig. 4, the gradient of cosine similarity is indeed more prone to producing large values. This issue becomes more pronounced as the model scales up.

## 5. Experiments

In this section, we validate the effectiveness of *Fractal-IR* on 7 IR tasks, *i.e.*, image SR, image Dn, JPEG image compression artifact removal (JPEG CAR), single-image motion deblurring, defocus deblurring and image demosaicking, and IR in adverse weather conditions (AWC). More details about the training protocols and the training/test datasets are shown in Appx. 1. The best and the second-best quantitative results are reported in red and blue.

### 5.1. Ablation Studies

**Effect of  $\mathcal{L}_1$  and  $\mathcal{L}_2$  information flow.** One design choice for the  $\mathcal{L}_1/\mathcal{L}_2$  information flow attentions is to decide whether to interleave them across transformer layers or to implement them in the same layer. To validate this choice, we develop three versions (Fig. C, Appx. 4), including v1 where  $\mathcal{L}_1$  and  $\mathcal{L}_2$  attentions alternate in consecutive layers, v2 and v3 where  $\mathcal{L}_1$  and  $\mathcal{L}_2$  attentions are used in the same layer. Compared with v1, v2 showed reduced performance despite increased model complexity. To address this issue, we introduce v3, where the projection layer between  $\mathcal{L}_1$  and  $\mathcal{L}_2$  is removed and the dimension of  $Q$  and  $K$  in

Table 6. Ablation study on model design with SR.

Scale	L1/L2 Version	L3 Version			
		Model size [M]		PSNR	
		with L3	w/o L3	with L3	w/o L3
2×	v1	14.35	11.87	38.34	38.31
2×	v2	19.22	16.74	38.30	38.22
2×	v3	15.69	13.21	38.37	38.35
2×	v4	17.19	-	38.41	-

Table 7. Model efficiency vs. accuracy for SR and Dn. PSNR is reported on Urban100 dataset.

Task	Network	Arch.	Params FLOPs Runtime PSNR			
			[M]	[G]	[ms]	[dB]
4× SR	SwinIR [52]	Columnar	11.90	215.32	152.24	27.45
	CAT [13]	Columnar	16.60	387.86	357.97	27.89
	HAT [11]	Columnar	20.77	416.90	368.61	28.37
	Fractal-IR (Ours)	Columnar	14.83	287.20	331.92	28.44
Dn 50	SwinIR [52]	Columnar	11.50	804.66	1772.84	27.98
	Restormer [93]	U-shape	26.13	154.88	210.44	28.29
	GRL [48]	Columnar	19.81	1361.77	3944.17	28.59
	Fractal-IR (Ours)	U-shape	22.33	153.66	399.05	28.91

$\mathcal{L}_1/\mathcal{L}_2$  attention is reduced by half to save computational complexities. Our ablation study reveals that v3 yielded the best performance, as evidenced by the results in Tab. 6. Thus, v3 was adopted for all subsequent experiments.

**Effect of the depth of the fractal structure.** Ablation study was conducted to evaluate the effect of the tree structure’s depth. In Tab. 6, the depth of the tree in the v1 model is 3. Removing the  $\mathcal{L}_3$  information flow reduces the depth to 2, resulting in degraded image SR performance, even on the small Set5 dataset. Additionally, a v4 model was designed by adding an information flow attention beyond  $\mathcal{L}_2$  to v3 model, creating a depth-4 fractal structure. As shown in Tab. 6, this increased complexity improves SR results. Thus, well-designed deeper tree structures lead to improved model performance but with increased model complexity.

**Efficiency Analysis.** We report the efficiency comparison results on 4× SR and denoising in Tab. 7. For the columnar architecture-based SR, our *Fractal-IR* achieves the best PSNR with much lower parameters (28.6% reduction) and FLOPs (31.1% reduction), and runtime (9.95% reduction) compared to HAT [11]. Similar observation can also be achieved on the denoising task.

### 5.2. Evaluation of *Fractal-IR* on Various IR tasks

**Image SR.** For the classical image SR, we compared our *Fractal-IR* with state-of-the-art SR models. The quantitative results are shown in Tab. 8. More results are shown in Fig. D of Appx. 5. Aside from the 2nd-best PSNR on Set5 and Set14, the proposed *Fractal-IR* archives the best PSNR and SSIM on all other test sets. In particular, significant improvements in terms of the PSNR on Urban100 (*i.e.*, 0.13 dB for 2× SR of the base model) and Manga109 (*i.e.*, 0.21 dB for 2× SR of the large model) compared to HAT [11], but with fewer trainable parameters. The visual

Table 8. *Classical image SR* results. Top-2 results are highlighted in red and blue.

Method	Scale	Params [M]	Set5		Set14		BSD100		Urban100		Manga109	
			PSNR↑	SSIM↑	PSNR↑	SSIM↑	PSNR↑	SSIM↑	PSNR↑	SSIM↑	PSNR↑	SSIM↑
EDSR [53]	2×	40.73	38.11	0.9602	33.92	0.9195	32.32	0.9013	32.93	0.9351	39.10	0.9773
RCAN [103]	2×	15.44	38.27	0.9614	34.12	0.9216	32.41	0.9027	33.34	0.9384	39.44	0.9786
SAN [18]	2×	15.71	38.31	0.9620	34.07	0.9213	32.42	0.9028	33.10	0.9370	39.32	0.9792
NLSA [65]	2×	42.63	38.34	0.9618	34.08	0.9231	32.43	0.9027	33.42	0.9394	39.59	0.9789
IPT [9]	2×	115.48	38.37	-	34.43	-	32.48	-	33.76	-	-	-
SwinIR [52]	2×	11.75	38.42	0.9623	34.46	0.9250	32.53	0.9041	33.81	0.9427	39.92	0.9797
CAT-A [13]	2×	16.46	38.51	0.9626	34.78	0.9265	32.59	0.9047	34.26	0.9440	40.10	0.9805
ART [95]	2×	16.40	38.56	0.9629	34.59	0.9267	32.58	0.9048	34.3	0.9452	40.24	0.9808
EDT [47]	2×	11.48	38.63	0.9632	34.80	0.9273	32.62	0.9052	34.27	0.9456	40.37	0.9811
GRL-B [48]	2×	20.05	38.67	0.9647	35.08	<b>0.9303</b>	32.67	<b>0.9087</b>	35.06	<b>0.9505</b>	40.67	0.9818
HAT [11]	2×	20.62	38.73	0.9637	35.13	0.9282	32.69	0.9060	34.81	<b>0.9489</b>	40.71	0.9819
Fractal-IR-B	2×	14.68	38.71	<b>0.9657</b>	35.16	0.9299	32.73	<b>0.9087</b>	34.94	0.9484	40.81	0.9830
HAT-L [11]	2×	40.70	<b>38.91</b>	0.9646	<b>35.29</b>	0.9293	<b>32.74</b>	0.9066	<b>35.09</b>	<b>0.9505</b>	<b>41.01</b>	<b>0.9831</b>
Fractal-IR-L	2×	39.07	<b>38.87</b>	<b>0.9663</b>	<b>35.27</b>	<b>0.9311</b>	<b>32.77</b>	<b>0.9092</b>	<b>35.16</b>	<b>0.9505</b>	<b>41.22</b>	<b>0.9846</b>

Table 10. *Color and grayscale image denoising* results.

Method	Params [M]	Color						Grayscale								
		CBSD68 [63]			McMaster [102]			Urban100 [30]			Set12 [97]			Urban100 [30]		
		$\sigma=15$	$\sigma=25$	$\sigma=50$	$\sigma=15$	$\sigma=25$	$\sigma=50$	$\sigma=15$	$\sigma=25$	$\sigma=50$	$\sigma=15$	$\sigma=25$	$\sigma=50$	$\sigma=15$	$\sigma=25$	$\sigma=50$
DnCNN [35]	0.56	33.90	31.24	27.95	33.45	31.52	28.62	32.98	30.81	27.59	32.86	30.44	27.18	32.64	29.95	26.26
IPT [9]	115.33	-	-	28.39	-	-	29.98	-	-	29.71	-	-	-	-	-	-
EDT-B [47]	11.48	34.39	31.76	28.56	35.61	33.34	30.25	35.22	33.07	30.16	-	-	-	-	-	-
SwinIR [52]	11.75	34.42	31.78	28.56	35.61	33.20	30.22	35.13	32.90	29.82	33.36	31.01	27.91	33.70	31.30	27.98
Restormer [93]	26.13	34.40	31.79	28.60	35.61	33.34	30.30	35.13	32.96	30.02	33.42	31.08	28.00	33.79	31.46	28.29
Xformer [96]	25.23	<b>34.43</b>	<b>31.82</b>	<b>28.63</b>	<b>35.68</b>	<b>33.44</b>	<b>30.38</b>	<b>35.29</b>	<b>33.21</b>	<b>30.36</b>	<b>33.46</b>	<b>31.16</b>	<b>28.10</b>	<b>33.98</b>	<b>31.78</b>	<b>28.71</b>
Fractal-IR	22.33	<b>34.42</b>	<b>31.82</b>	<b>28.62</b>	<b>35.69</b>	<b>33.44</b>	<b>30.42</b>	<b>35.46</b>	<b>33.34</b>	<b>30.59</b>	<b>33.48</b>	<b>31.19</b>	<b>28.15</b>	<b>34.11</b>	<b>31.92</b>	<b>28.91</b>

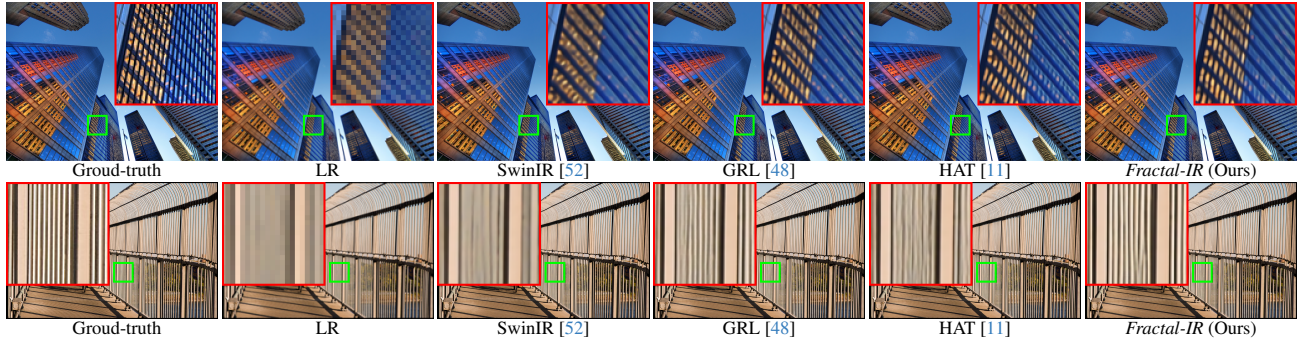


Figure 5. Visual results for classical image  $\times 4$  SR on Urban100 dataset.

results shown in Fig. 5 also validate the effectiveness of the proposed *Fractal-IR* in restoring more structural content.

**Image Denoising.** We provide both color and grayscale image denoising results in Tab. 10. Our approach demonstrates superior performance on diverse datasets, including McMaster, and Urban100 for color images, as well as Set12 and Urban100 for grayscale images. For grayscale image denoising with  $\sigma = 50$ , *Fractal-IR* improves the PSNR on Set12 and Urban100 by 0.05dB and 0.20dB compared with Xformer. It is noteworthy that our method outperforms DRUNet, Restormer, and Xformer, despite utilizing fewer trainable parameters. Additionally, a closer examination of more visual results is available in the appendix, further substantiates the capabilities of *Fractal-IR*. These results illustrate its proficiency in effectively eliminating heavy noise corruption while preserving high-frequency image details.

**Image JPEG CAR.** For JPEG CAR, the experiments are conducted for color and grayscale images with four qual-

Table 9. *Single-image motion deblurring* on GoPro and HIDE dataset. GoPro dataset is used for training.

Method	GoPro	HIDE	Average
	PSNR↑ / SSIM↑	PSNR↑ / SSIM↑	PSNR↑ / SSIM↑
DeblurGAN [38]	28.70 / 0.858	24.51 / 0.871	26.61 / 0.865
Nah <i>et al.</i> [66]	29.08 / 0.914	25.73 / 0.874	27.41 / 0.894
DeblurGAN-v2 [39]	29.55 / 0.934	26.61 / 0.875	28.08 / 0.905
SRN [80]	30.26 / 0.934	28.36 / 0.915	29.31 / 0.925
SPAIR [70]	32.06 / 0.953	30.29 / 0.931	31.18 / 0.942
MIMO-UNet+ [14]	32.45 / 0.957	29.99 / 0.930	31.22 / 0.944
MPRNet [92]	32.66 / 0.959	30.96 / 0.939	31.81 / 0.949
MAXIM-3S [83]	32.86 / 0.961	32.83 / 0.956	32.85 / 0.959
Restormer [93]	32.92 / 0.961	31.22 / 0.942	32.07 / 0.952
Stripformer [81]	33.08 / 0.962	31.03 / 0.940	32.06 / 0.951
ShuffleFormer [89]	33.38 / <b>0.965</b>	31.25 / 0.943	31.32 / 0.954
GRL-B [48]	<b>33.93 / 0.968</b>	<b>31.65 / 0.947</b>	<b>32.79 / 0.958</b>
Fractal-IR-L	<b>33.99 / 0.968</b>	<b>31.64 / 0.947</b>	<b>32.82 / 0.958</b>

Table 11. *Dual-pixel defocus deblurring.*

Method	Combined Scenes			
	PSNR↑	SSIM↑	MAE↓	LPIPS↓
DPDNet [1]	25.13	0.786	0.041	0.223
RDPD [2]	25.39	0.772	0.040	0.255
Uformer [88]	25.65	0.795	0.039	0.243
IFAN [42]	25.99	0.804	0.037	0.207
Restormer [93]	<b>26.66</b>	<b>0.833</b>	<b>0.035</b>	<b>0.155</b>
Fractal-IR-B	<b>27.01</b>	<b>0.848</b>	<b>0.034</b>	<b>0.135</b>

ity factors (QF) (*i.e.*, 10, 20, 30, and 40). The results for grayscale and color images are shown in Tab. 12 and the Tab. E of Appx. 5. The quantitative results validate that the proposed *Fractal-IR* outperforms most of the other comparison methods (Refer to the visual results in Fig. 8 on LIVE1 dataset). More visual comparisons are provided in the Appendix to further support the effectiveness of *Fractal-IR*.

We also trained the model to handle multiple degradation levels. The results in Tab. 12 show that *Fractal-IR* outperforms DRUNet for grayscale image JPEG CAR by a large margin under this setting. Fig. 6 shows the results for denoising in noise range [15, 75] and JPEG CAR in QF range [10, 90]. Despite that only one model is trained, the model performs well on different degradation levels.

**Single-Image Motion Deblurring.** The results regarding the single-image motion deblurring are shown in Tab. 9. Compared with previous state-of-the-art GRL [48], the proposed *Fractal-IR* achieves the best results on the GoPro

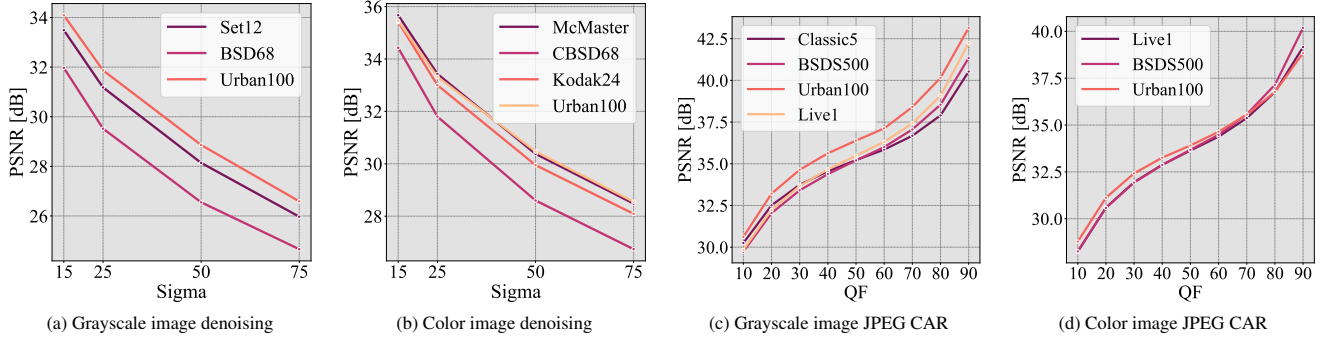


Figure 6. Training one model for multiple degradation levels of image denoising and JPEG compression artifact removal.

Table 12. *Grayscale image JPEG compression artifact removal* results. †A single model is trained to handle multiple noise levels.

Set	QF	JPEG		†DRUNet [100]		†Fractal-IR		SwinIR [52]		ART [95]		CAT [13]		Fractal-IR	
		PSNR↑	SSIM↑	PSNR↑	SSIM↑	PSNR↑	SSIM↑	PSNR↑	SSIM↑	PSNR↑	SSIM↑	PSNR↑	SSIM↑	PSNR↑	SSIM↑
Classic5	10	27.82	0.7600	<b>30.16</b>	<b>0.8234</b>	<b>30.25</b>	<b>0.8236</b>	<b>30.27</b>	0.8249	<b>30.27</b>	<b>0.8258</b>	30.26	<b>0.8250</b>	<b>30.38</b>	<b>0.8266</b>
	20	30.12	0.8340	<b>32.39</b>	<b>0.8734</b>	<b>32.51</b>	<b>0.8737</b>	32.52	0.8748	-	-	<b>32.57</b>	<b>0.8754</b>	<b>32.62</b>	<b>0.8751</b>
	30	31.48	0.8670	<b>33.59</b>	<b>0.8949</b>	<b>33.74</b>	<b>0.8954</b>	33.73	0.8961	33.74	<b>0.8964</b>	<b>33.77</b>	<b>0.8964</b>	<b>33.80</b>	<b>0.8962</b>
	40	32.43	0.8850	<b>34.41</b>	<b>0.9075</b>	<b>34.55</b>	<b>0.9078</b>	34.52	0.9082	34.55	<b>0.9086</b>	34.58	<b>0.9087</b>	<b>34.61</b>	<b>0.9082</b>
LIVE1	10	27.77	0.7730	<b>29.79</b>	<b>0.8278</b>	<b>29.84</b>	<b>0.8328</b>	29.86	0.8287	<b>29.89</b>	<b>0.8300</b>	<b>29.89</b>	0.8295	<b>29.94</b>	<b>0.8359</b>
	20	30.07	0.8510	<b>32.17</b>	<b>0.8899</b>	<b>32.24</b>	<b>0.8926</b>	32.25	0.8909	-	-	<b>32.30</b>	<b>0.8913</b>	<b>32.31</b>	<b>0.8938</b>
	30	31.41	0.8850	<b>33.59</b>	<b>0.9166</b>	<b>33.67</b>	<b>0.9192</b>	33.69	0.9174	<b>33.71</b>	<b>0.9178</b>	<b>33.73</b>	0.9177	<b>33.73</b>	<b>0.9223</b>
	40	32.35	0.9040	<b>34.58</b>	<b>0.9312</b>	<b>34.66</b>	<b>0.9347</b>	34.67	0.9317	34.70	<b>0.9322</b>	<b>34.72</b>	0.9320	<b>34.71</b>	<b>0.9347</b>
Urban100	10	26.33	0.7816	<b>30.31</b>	<b>0.8745</b>	<b>30.62</b>	<b>0.8808</b>	30.55	0.8835	<b>30.87</b>	<b>0.8894</b>	30.81	0.8866	<b>31.07</b>	<b>0.8950</b>
	20	28.57	0.8545	<b>32.81</b>	<b>0.9241</b>	<b>33.21</b>	<b>0.9256</b>	33.12	0.9190	-	-	33.38	<b>0.9269</b>	<b>33.51</b>	<b>0.9250</b>
	30	30.00	0.9013	<b>34.23</b>	<b>0.9414</b>	<b>34.64</b>	<b>0.9478</b>	34.58	0.9417	<b>34.81</b>	<b>0.9442</b>	<b>34.81</b>	<b>0.9449</b>	<b>34.86</b>	<b>0.9459</b>
	40	31.06	0.9215	<b>35.20</b>	<b>0.9547</b>	<b>35.63</b>	<b>0.9566</b>	35.50	0.9515	<b>35.73</b>	<b>0.9553</b>	<b>35.73</b>	0.9511	<b>35.77</b>	<b>0.9561</b>

Table 13. *Image demosaicking* results.

Datasets	Matlab	RLDD [29]	DRUNet [100]	RNAN [104]	GRL-S [48]	Ours
Kodak	35.78	42.49	42.68	43.16	<b>43.57</b>	<b>43.69</b>
McMaster	34.43	39.25	39.39	39.70	<b>40.22</b>	<b>40.78</b>

Table 14. *IR in AWC* results.

Dataset	All-in-One [45]	TransWeather [84]	SemanIR [72]	Ours
RainDrop [71]	<b>31.12</b>	28.84	30.82	<b>30.84</b>
Test1 (rain+fog) [45]	24.71	27.96	<b>29.57</b>	<b>30.93</b>
SnowTest100k-L [56]	28.33	28.48	<b>30.76</b>	<b>30.85</b>



Figure 7. Visual results for single image motion deblurring on GoPro dataset.

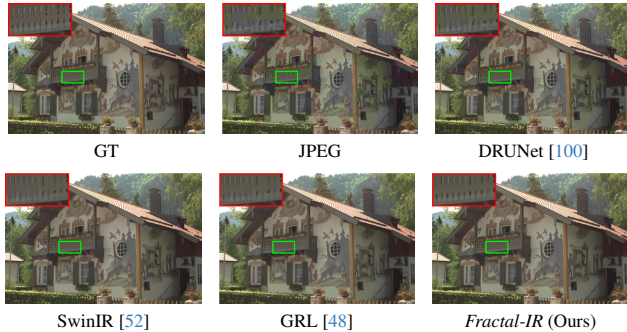


Figure 8. Visual results for JPEG CAR on LIVE1 dataset

dataset (See visual results in Fig. 7) and the second-best results on HIDE datasets. More The results on RealBlur [73] dataset and more visual results are shown in the Appendix. **Defocus Deblurring.** We also validate the effectiveness of our *Fractal-IR* for dual-pixel defocus deblurring. The results in Tab. 11 show that *Fractal-IR* outperforms the previous methods. Compared with Restormer on the combined scenes, our *Fractal-IR* achieves a decent performance boost of 0.35 dB for dual-pixel defocus deblurring.

**Image Demosaicking.** We compare *Fractal-IR* with the other methods for demosaicking in Tab. 13. It shows that the proposed *Fractal-IR* archives the best performance on both the Kodak and MaMaster test datasets, especially, 0.12 dB and 0.56 dB absolute improvement compared to GRL.

**IR in AWC.** We validate *Fractal-IR* in adverse weather conditions like rain, fog, and snow. We compare *Fractal-IR* with three methods in Tab. 14. Our method achieves the best performance on Test1 (*i.e.*, 4.6% improvement) and SnowTest100k-L (*i.e.*, 0.09 dB improvement), while the second-best PSNR on RainDrop compared to all other methods. The visual result in the Appendix shows that *Fractal-IR* can remove more adverse weather artifacts.

## 6. Conclusion

In this paper, we introduced a fractal information flow principle for image restoration. Leveraging this concept, we devised a new model called *Fractal-IR*, which progressively propagates information within local regions, facilitates information exchange in non-local ranges, and mitigates in-



formation isolation in the global context. We investigated how to scale up an IR model. The effectiveness and generalizability of *Fractal-IR* were validated through comprehensive experiments across various IR tasks.

## References

- [1] Abdullah Abuolaim and Michael S Brown. Defocus deblurring using dual-pixel data. In *ECCV*, pages 111–126. Springer, 2020. 7, 14, 18
- [2] Abdullah Abuolaim, Mauricio Delbracio, Damien Kelly, Michael S. Brown, and Peyman Milanfar. Learning to reduce defocus blur by realistically modeling dual-pixel data. In *ICCV*, 2021. 7, 18
- [3] Eirikur Agustsson and Radu Timofte. NTIRE 2017 challenge on single image super-resolution: Dataset and study. In *CVPRW*, pages 126–135, 2017. 3, 13, 14
- [4] Saeed Anwar and Nick Barnes. Densely residual laplacian super-resolution. *IEEE TPAMI*, 44(3):1192–1204, 2020. 2
- [5] Pablo Arbelaez, Michael Maire, Charless Fowlkes, and Jitendra Malik. Contour detection and hierarchical image segmentation. *IEEE TPAMI*, 33(5):898–916, 2010. 13
- [6] Danielle S Bassett, Andreas Meyer-Lindenberg, Sophie Achard, Thomas Duke, and Edward Bullmore. Adaptive reconfiguration of fractal small-world human brain functional networks. *Proceedings of the National Academy of Sciences*, 103(51):19518–19523, 2006. 2
- [7] Marco Bevilacqua, Aline Roumy, Christine Guillemot, and Marie Line Alberi-Morel. Low-complexity single-image super-resolution based on nonnegative neighbor embedding. In *BMVC*, 2012. 13
- [8] Antoni Buades, Bartomeu Coll, and J-M Morel. A non-local algorithm for image denoising. In *CVPR*, pages 60–65, 2005. 2
- [9] Hanting Chen, Yunhe Wang, Tianyu Guo, Chang Xu, Yiping Deng, Zhenhua Liu, Siwei Ma, Chunjing Xu, Chao Xu, and Wen Gao. Pre-trained image processing transformer. In *CVPR*, pages 12299–12310, 2021. 1, 2, 3, 7, 13, 16
- [10] Liangyu Chen, Xiaojie Chu, Xiangyu Zhang, and Jian Sun. Simple baselines for image restoration. In *ECCV*, pages 17–33. Springer, 2022. 4
- [11] Xiangyu Chen, Xintao Wang, Jiantao Zhou, Yu Qiao, and Chao Dong. Activating more pixels in image super-resolution transformer. In *CVPR*, pages 22367–22377, 2023. 2, 3, 5, 6, 7, 13, 15, 16
- [12] Yunjin Chen and Thomas Pock. Trainable nonlinear reaction diffusion: A flexible framework for fast and effective image restoration. *IEEE TPAMI*, 39(6):1256–1272, 2016. 2
- [13] Zheng Chen, Yulun Zhang, Jinjin Gu, Linghe Kong, Xin Yuan, et al. Cross aggregation transformer for image restoration. *NeurIPS*, 35:25478–25490, 2022. 2, 6, 7, 8, 16
- [14] Sung-Jin Cho, Seo-Won Ji, Jun-Pyo Hong, Seung-Won Jung, and Sung-Jea Ko. Rethinking coarse-to-fine approach in single image deblurring. In *ICCV*, 2021. 7, 17
- [15] Xiangxiang Chu, Zhi Tian, Bo Zhang, Xinlong Wang, and Chunhua Shen. Conditional positional encodings for vision transformers. In *ICLR*, 2022. 4
- [16] Marcos V Conde, Ui-Jin Choi, Maxime Burchi, and Radu Timofte. Swin2SR: SwinV2 transformer for compressed image super-resolution and restoration. In *ECCVW*, pages 669–687, 2022. 2
- [17] Kostadin Dabov, Alessandro Foi, Vladimir Katkovnik, and Karen Egiazarian. Image denoising by sparse 3-d transform-domain collaborative filtering. *IEEE TIP*, 16(8):2080–2095, 2007. 2
- [18] Tao Dai, Jianrui Cai, Yongbing Zhang, Shu-Tao Xia, and Lei Zhang. Second-order attention network for single image super-resolution. In *CVPR*, pages 11065–11074, 2019. 7, 16
- [19] Jia Deng, Wei Dong, Richard Socher, Li-Jia Li, Kai Li, and Li Fei-Fei. ImageNet: A large-scale hierarchical image database. In *CVPR*, pages 248–255. IEEE, 2009. 13
- [20] Chao Dong, Chen Change Loy, Kaiming He, and Xiaoou Tang. Learning a deep convolutional network for image super-resolution. In *ECCV*, pages 184–199. Springer, 2014. 1, 2, 13
- [21] Alexey Dosovitskiy, Lucas Beyer, Alexander Kolesnikov, Dirk Weissenborn, Xiaohua Zhai, Thomas Unterthiner, Mostafa Dehghani, Matthias Minderer, Georg Heigold, Sylvain Gelly, et al. An image is worth 16x16 words: Transformers for image recognition at scale. *arXiv preprint arXiv:2010.11929*, 2020. 3
- [22] Sina Farsiu, M Dirk Robinson, Michael Elad, and Peyman Milanfar. Fast and robust multiframe super resolution. *IEEE TIP*, 13(10):1327–1344, 2004. 2
- [23] Alessandro Foi, Vladimir Katkovnik, and Karen Egiazarian. Pointwise shape-adaptive dct for high-quality denoising and deblocking of grayscale and color images. *IEEE TIP*, 16(5):1395–1411, 2007. 13
- [24] Rich Franzen. Kodak lossless true color image suite. *source: http://r0k.us/graphics/kodak*, 4(2), 1999. 13, 14
- [25] P Goyal. Accurate, large minibatch sg d: training imagenet in 1 hour. *arXiv preprint arXiv:1706.02677*, 2017. 5
- [26] Albert Gu and Tri Dao. Mamba: Linear-time sequence modeling with selective state spaces. *arXiv preprint arXiv:2312.00752*, 2023. 2
- [27] Shuhang Gu, Lei Zhang, Wangmeng Zuo, and Xiangchu Feng. Weighted nuclear norm minimization with application to image denoising. In *CVPR*, pages 2862–2869, 2014. 2
- [28] Hang Guo, Jinmin Li, Tao Dai, Zhihao Ouyang, Xudong Ren, and Shu-Tao Xia. MambaIR: A simple baseline for image restoration with state-space model. *arXiv preprint arXiv:2402.15648*, 2024. 1, 2
- [29] Yu Guo, Qiyu Jin, Gabriele Facciolo, Tiejong Zeng, and Jean-Michel Morel. Residual learning for effective joint demosaicing-denoising. *arXiv preprint arXiv:2009.06205*, 2020. 8
- [30] Jia-Bin Huang, Abhishek Singh, and Narendra Ahuja. Single image super-resolution from transformed self-exemplars. In *CVPR*, pages 5197–5206, 2015. 7, 13

- [31] Zilong Huang, Youcheng Ben, Guozhong Luo, Pei Cheng, Gang Yu, and Bin Fu. Shuffle transformer: Rethinking spatial shuffle for vision transformer. *arXiv preprint arXiv:2106.03650*, 2021. 3, 4, 16, 17
- [32] Justin Johnson, Alexandre Alahi, and Li Fei-Fei. Perceptual losses for real-time style transfer and super-resolution. In *ECCV*, pages 694–711. Springer, 2016. 13
- [33] Dayal Singh Kalra and Maissam Barkeshli. Why warmup the learning rate? underlying mechanisms and improvements. *arXiv preprint arXiv:2406.09405*, 2024. 5
- [34] Ali Karaali and Claudio Rosito Jung. Edge-based defocus blur estimation with adaptive scale selection. *TIP*, 2017. 18
- [35] Daisuke Kiku, Yusuke Monno, Masayuki Tanaka, and Masatoshi Okutomi. Beyond color difference: Residual interpolation for color image demosaicking. *IEEE TIP*, 25(3):1288–1300, 2016. 7, 18
- [36] Kiyeon Kim, Seungyong Lee, and Sunghyun Cho. MSS-Net: Multi-scale-stage network for single image deblurring. In *ECCVW*, pages 524–539. Springer, 2022. 17
- [37] Diederik P Kingma and Jimmy Ba. Adam: A method for stochastic optimization. *arXiv preprint arXiv:1412.6980*, 2014. 13
- [38] Orest Kupyn, Volodymyr Budzan, Mykola Mykhailych, Dmytro Mishkin, and Jiří Matas. DeblurGAN: Blind motion deblurring using conditional adversarial networks. In *CVPR*, 2018. 7
- [39] Orest Kupyn, Tetiana Martyniuk, Junru Wu, and Zhangyang Wang. DeblurGAN-v2: Deblurring (orders-of-magnitude) faster and better. In *ICCV*, 2019. 7
- [40] Gustav Larsson, Michael Maire, and Gregory Shakhnarovich. FractalNet: Ultra-deep neural networks without residuals. *arXiv preprint arXiv:1605.07648*, 2016. 2
- [41] Junyong Lee, Sungkil Lee, Sunghyun Cho, and Seungyong Lee. Deep defocus map estimation using domain adaptation. In *CVPR*, 2019. 18
- [42] Junyong Lee, Hyeongseok Son, Jaesung Rim, Sunghyun Cho, and Seungyong Lee. Iterative filter adaptive network for single image defocus deblurring. In *CVPR*, 2021. 7, 18
- [43] Anat Levin, Yair Weiss, Fredo Durand, and William T. Freeman. Understanding and evaluating blind deconvolution algorithms. In *CVPR*, pages 1964–1971, 2009. 2
- [44] Ruoteng Li, Loong-Fah Cheong, and Robby T Tan. Heavy rain image restoration: Integrating physics model and conditional adversarial learning. In *CVPR*, pages 1633–1642, 2019. 13, 14
- [45] Ruoteng Li, Robby T Tan, and Loong-Fah Cheong. All in one bad weather removal using architectural search. In *CVPR*, pages 3175–3185, 2020. 8, 14
- [46] Tianhong Li, Qinyi Sun, Lijie Fan, and Kaiming He. Fractal generative models. *arXiv preprint arXiv:2502.17437*, 2025. 2, 3
- [47] Wenbo Li, Xin Lu, Jiangbo Lu, Xiangyu Zhang, and Jiaya Jia. On efficient transformer and image pre-training for low-level vision. *arXiv preprint arXiv:2112.10175*, 2021. 3, 7, 13, 16
- [48] Yawei Li, Yuchen Fan, Xiaoyu Xiang, Denis Demandolx, Rakesh Ranjan, Radu Timofte, and Luc Van Gool. Efficient and explicit modelling of image hierarchies for image restoration. In *CVPR*, pages 18278–18289, 2023. 2, 3, 4, 6, 7, 8, 16, 17
- [49] Yawei Li, Kai Zhang, Jingyun Liang, Jie Zhang Cao, Ce Liu, Rui Gong, Yulun Zhang, Hao Tang, Yun Liu, Denis Demandolx, et al. LSDIR: A large scale dataset for image restoration. In *CVPRW*, pages 1775–1787, 2023. 3
- [50] Zhen Li, Jinglei Yang, Zheng Liu, Xiaomin Yang, Gwanggil Jeon, and Wei Wu. Feedback network for image super-resolution. In *CVPR*, pages 3867–3876, 2019. 16
- [51] Zheyuan Li, Yingqi Liu, Xiangyu Chen, Haoming Cai, Jinjin Gu, Yu Qiao, and Chao Dong. Blueprint separable residual network for efficient image super-resolution. In *CVPR*, pages 833–843, 2022. 2
- [52] Jingyun Liang, Jie Zhang Cao, Guolei Sun, Kai Zhang, Luc Van Gool, and Radu Timofte. SwinIR: Image restoration using swin transformer. In *ICCVW*, pages 1833–1844, 2021. 1, 2, 3, 6, 7, 8, 16
- [53] Bee Lim, Sanghyun Son, Heewon Kim, Seungjun Nah, and Kyoung Mu Lee. Enhanced deep residual networks for single image super-resolution. In *CVPRW*, pages 1132–1140, 2017. 1, 2, 5, 7, 13, 14, 15, 16
- [54] Ding Liu, Bihan Wen, Yuchen Fan, Chen Change Loy, and Thomas S Huang. Non-local recurrent network for image restoration. *arXiv preprint arXiv:1806.02919*, 2018. 3
- [55] Ding Liu, Bihan Wen, Yuchen Fan, Chen Change Loy, and Thomas S Huang. Non-local recurrent network for image restoration. *NeurIPS*, 31, 2018. 3
- [56] Yun-Fu Liu, Da-Wei Jaw, Shih-Chia Huang, and Jenq-Neng Hwang. DesnowNet: Context-aware deep network for snow removal. *IEEE TIP*, 27(6):3064–3073, 2018. 8, 13
- [57] Ze Liu, Yutong Lin, Yue Cao, Han Hu, Yixuan Wei, Zheng Zhang, Stephen Lin, and Baining Guo. Swin transformer: Hierarchical vision transformer using shifted windows. In *ICCV*, pages 10012–10022, 2021. 3, 5
- [58] Ze Liu, Han Hu, Yutong Lin, Zhuliang Yao, Zhenda Xie, Yixuan Wei, Jia Ning, Yue Cao, Zheng Zhang, Li Dong, et al. Swin transformer v2: Scaling up capacity and resolution. In *CVPR*, pages 12009–12019, 2022. 3, 5
- [59] Ilya Loshchilov and Frank Hutter. Decoupled weight decay regularization. In *ICLR*, 2018. 13
- [60] Kede Ma, Zhengfang Duanmu, Qingbo Wu, Zhou Wang, Hongwei Yong, Hongliang Li, and Lei Zhang. Waterloo exploration database: New challenges for image quality assessment models. *IEEE TIP*, 26(2):1004–1016, 2016. 13
- [61] Henrique S Malvar, Li-wei He, and Ross Cutler. High-quality linear interpolation for demosaicing of bayer-patterned color images. In *IEEE International Conference on Acoustics, Speech, and Signal Processing*, pages iii–485. IEEE, 2004. 2
- [62] Xintian Mao, Yiming Liu, Fengze Liu, Qingli Li, Wei Shen, and Yan Wang. Intriguing findings of frequency selection for image deblurring. In *AAAI*, pages 1905–1913, 2023. 17
- [63] David Martin, Charless Fowlkes, Doron Tal, and Jitendra Malik. A database of human segmented natural images and

- its application to evaluating segmentation algorithms and measuring ecological statistics. In *ICCV*, pages 416–423. IEEE, 2001. 7, 13
- [64] Yusuke Matsui, Kota Ito, Yuji Aramaki, Azuma Fujimoto, Toru Ogawa, Toshihiko Yamasaki, and Kiyoharu Aizawa. Sketch-based manga retrieval using manga109 dataset. *Multimedia Tools and Applications*, 76(20):21811–21838, 2017. 13
- [65] Yiqun Mei, Yuchen Fan, and Yuqian Zhou. Image super-resolution with non-local sparse attention. In *CVPR*, pages 3517–3526, 2021. 3, 7, 16
- [66] Seungjun Nah, Tae Hyun Kim, and Kyoung Mu Lee. Deep multi-scale convolutional neural network for dynamic scene deblurring. In *CVPR*, pages 3883–3891, 2017. 7, 14
- [67] Ben Niu, Weilei Wen, Wenqi Ren, Xiangde Zhang, Lianping Yang, Shuzhen Wang, Kaihao Zhang, Xiaochun Cao, and Haifeng Shen. Single image super-resolution via a holistic attention network. In *ECCV*, pages 191–207, 2020. 16
- [68] Jinshan Pan, Zhe Hu, Zhixun Su, and Ming-Hsuan Yang. Deblurring text images via l0-regularized intensity and gradient prior. In *CVPR*, pages 2901–2908, 2014. 2
- [69] Matan Protter, Michael Elad, Hiroyuki Takeda, and Peyman Milanfar. Generalizing the nonlocal-means to super-resolution reconstruction. *IEEE TIP*, 18(1):36–51, 2008. 2
- [70] Kuldeep Purohit, Maitreya Suin, AN Rajagopalan, and Vishnu Naresh Boddeti. Spatially-adaptive image restoration using distortion-guided networks. In *ICCV*, 2021. 7
- [71] Rui Qian, Robby T Tan, Wenhan Yang, Jiajun Su, and Jiaying Liu. Attentive generative adversarial network for rain-drop removal from a single image. In *CVPR*, pages 2482–2491, 2018. 8, 13, 14
- [72] Bin Ren, Yawei Li, Jingyun Liang, Rakesh Ranjan, Mengyuan Liu, Rita Cucchiara, Luc Van Gool, Ming-Hsuan Yang, and Nicu Sebe. Sharing key semantics in transformer makes efficient image restoration. In *NeurIPS*, 2024. 3, 4, 8
- [73] Jaesung Rim, Haeyun Lee, Jucheol Won, and Sunghyun Cho. Real-world blur dataset for learning and benchmarking deblurring algorithms. In *ECCV*, pages 184–201. Springer, 2020. 8, 14
- [74] Qi Shan, Jiaya Jia, and Aseem Agarwala. High-quality motion deblurring from a single image. *ACM Transactions on Graphics (TOG)*, 27(3):1–10, 2008. 2
- [75] HR Sheikh. Live image quality assessment database release 2. <http://live.ece.utexas.edu/research/quality>, 2005. 13
- [76] Ziyi Shen, Wenguan Wang, Xiankai Lu, Jianbing Shen, Haibin Ling, Tingfa Xu, and Ling Shao. Human-aware motion deblurring. In *ICCV*, pages 5572–5581, 2019. 14
- [77] Jianping Shi, Li Xu, and Jiaya Jia. Just noticeable defocus blur detection and estimation. In *CVPR*, 2015. 18
- [78] Karen Simonyan and Andrew Zisserman. Very deep convolutional networks for large-scale image recognition. In *ICLR*, 2015. 13
- [79] Hyeonseok Son, Junyong Lee, Sunghyun Cho, and Seungyong Lee. Single image defocus deblurring using kernel-sharing parallel atrous convolutions. In *ICCV*, 2021. 18
- [80] Xin Tao, Hongyun Gao, Xiaoyong Shen, Jue Wang, and Ji-aya Jia. Scale-recurrent network for deep image deblurring. In *CVPR*, 2018. 7, 17
- [81] Fu-Jen Tsai, Yan-Tsung Peng, Yen-Yu Lin, Chung-Chi Tsai, and Chia-Wen Lin. Stripformer: Strip transformer for fast image deblurring. In *ECCV*, pages 146–162. Springer, 2022. 7, 17
- [82] Fu-Jen Tsai, Yan-Tsung Peng, Chung-Chi Tsai, Yen-Yu Lin, and Chia-Wen Lin. BANet: A blur-aware attention network for dynamic scene deblurring. *IEEE TIP*, 31:6789–6799, 2022. 17
- [83] Zhengzhong Tu, Hossein Talebi, Han Zhang, Feng Yang, Peyman Milanfar, Alan Bovik, and Yinxiao Li. MAXIM: Multi-axis MLP for image processing. In *CVPR*, pages 5769–5780, 2022. 7, 17
- [84] Jeya Maria Jose Valanarasu, Rajeev Yasarla, and Vishal M Patel. TransWeather: Transformer-based restoration of images degraded by adverse weather conditions. In *CVPR*, pages 2353–2363, 2022. 8, 13
- [85] Ashish Vaswani, Noam Shazeer, Niki Parmar, Jakob Uszkoreit, Llion Jones, Aidan N Gomez, Łukasz Kaiser, and Illia Polosukhin. Attention is all you need. *NeurIPS*, 30, 2017. 3
- [86] Sinong Wang, Belinda Z Li, Madian Khabsa, Han Fang, and Hao Ma. Linformer: Self-attention with linear complexity. *arXiv preprint arXiv:2006.04768*, 2020. 3
- [87] Xintao Wang, Ke Yu, Shixiang Wu, Jinjin Gu, Yihao Liu, Chao Dong, Yu Qiao, and Chen Change Loy. ESRGAN: Enhanced super-resolution generative adversarial networks. In *ECCVW*, pages 0–0, 2018. 5
- [88] Zhendong Wang, Xiaodong Cun, Jianmin Bao, Wengang Zhou, Jianzhuang Liu, and Houqiang Li. Uformer: A general U-shaped transformer for image restoration. In *CVPR*, pages 17683–17693, 2022. 3, 7, 8, 18
- [89] Jie Xiao, Xueyang Fu, Man Zhou, Hongjian Liu, and Zheng-Jun Zha. Random shuffle transformer for image restoration. In *ICML*, pages 38039–38058, 2023. 3, 4, 7, 16
- [90] Yufei Xu, Qiming Zhang, Jing Zhang, and Dacheng Tao. Vitae: Vision transformer advanced by exploring intrinsic inductive bias. *NeurIPS*, 34:28522–28535, 2021. 4
- [91] Jianchao Yang, John Wright, Thomas Huang, and Yi Ma. Image super-resolution as sparse representation of raw image patches. In *CVPR*, pages 1–8, 2008. 2
- [92] Syed Waqas Zamir, Aditya Arora, Salman Khan, Munawar Hayat, Fahad Shahbaz Khan, Ming-Hsuan Yang, and Ling Shao. Multi-stage progressive image restoration. In *CVPR*, pages 14821–14831, 2021. 7, 8, 17
- [93] Syed Waqas Zamir, Aditya Arora, Salman Khan, Munawar Hayat, Fahad Shahbaz Khan, and Ming-Hsuan Yang. Restormer: Efficient transformer for high-resolution image restoration. In *CVPR*, pages 5728–5739, 2022. 2, 3, 6, 7, 8, 18
- [94] Roman Zeyde, Michael Elad, and Matan Protter. On single image scale-up using sparse-representations. In *Proceed-*

- ings of International Conference on Curves and Surfaces*, pages 711–730. Springer, 2010. [13](#)
- [95] Jiale Zhang, Yulun Zhang, Jinjin Gu, Yongbing Zhang, Linghe Kong, and Xin Yuan. Accurate image restoration with attention retractable transformer. In *ICLR, 2022*. [2](#), [7](#), [8](#), [16](#)
- [96] Jiale Zhang, Yulun Zhang, Jinjin Gu, Jiahua Dong, Linghe Kong, and Xiaokang Yang. Xformer: Hybrid x-shaped transformer for image denoising. *arXiv preprint arXiv:2303.06440*, 2023. [7](#)
- [97] Kai Zhang, Wangmeng Zuo, Yunjin Chen, Deyu Meng, and Lei Zhang. Beyond a Gaussian denoiser: residual learning of deep CNN for image denoising. *IEEE TIP*, 26(7):3142–3155, 2017. [2](#), [7](#), [13](#)
- [98] Kai Zhang, Wangmeng Zuo, Shuhang Gu, and Lei Zhang. Learning deep cnn denoiser prior for image restoration. In *CVPR*, pages 3929–3938, 2017. [18](#)
- [99] Kai Zhang, Wangmeng Zuo, and Lei Zhang. Ffdnet: Toward a fast and flexible solution for cnn-based image denoising. *IEEE TIP*, 27(9):4608–4622, 2018. [18](#)
- [100] Kai Zhang, Yawei Li, Wangmeng Zuo, Lei Zhang, Luc Van Gool, and Radu Timofte. Plug-and-play image restoration with deep denoiser prior. *IEEE TPAMI*, 2021. [8](#), [18](#)
- [101] Lei Zhang and Xiaolin Wu. Color demosaicking via directional linear minimum mean square-error estimation. *IEEE TIP*, 14(12):2167–2178, 2005. [2](#)
- [102] Lei Zhang, Xiaolin Wu, Antoni Buades, and Xin Li. Color demosaicking by local directional interpolation and nonlocal adaptive thresholding. *Journal of Electronic imaging*, 20(2):023016, 2011. [7](#), [13](#), [14](#)
- [103] Yulun Zhang, Kunpeng Li, Kai Li, Lichen Wang, Bineng Zhong, and Yun Fu. Image super-resolution using very deep residual channel attention networks. In *ECCV*, pages 286–301, 2018. [7](#), [16](#)
- [104] Yulun Zhang, Kunpeng Li, Kai Li, Bineng Zhong, and Yun Fu. Residual non-local attention networks for image restoration. *arXiv preprint arXiv:1903.10082*, 2019. [3](#), [8](#)

# Fractal-IR: A Unified Framework for Efficient and Scalable Image Restoration

## Supplementary Material

### 1. Experimental Settings

#### 1.1. Architecture Details

We choose two commonly used basic architectures for IR tasks including the U-shape hierarchical architecture and the columnar architecture. The columnar architecture is used for image SR while the U-shape architecture is used for other IR tasks including image denoising, JPEG CAR, image deblurring, IR in adverse weather conditions, image deblurring, and image demosaicking. We included details on the structure of the *Fractal-IR* in Tab. A. This table outlines the number of *Fractal-IR* stages and the distribution of *Fractal-IR* layers within each stage for a thorough understanding of our model’s architecture.

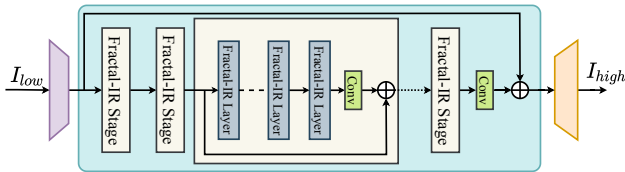


Figure A. The columnar *Fractal-IR* architecture.

#### 1.2. Training Details

The proposed *Fractal-IR* explores 7 different IR tasks, and the training settings vary slightly for each task. These differences encompass the architecture of the proposed *Fractal-IR*, variations in training phases, choice of the optimizer, employed loss functions, warm-up settings, learning rate schedules, batch sizes, and patch sizes. We have provided a comprehensive overview of these details.

In addition, there are several points about the training details we want to make further explanation. 1) For image SR, the network is pre-trained on ImageNet [19]. This is inspired by previous works [9, 11, 20, 47]. 2) The optimizer used for IR in AWC is Adam [37], while AdamW [59] is used for the rest IR tasks. 3) The training losses for IR in AWC are the smooth L1 and the Perception VGG loss [32, 78]. For image deblurring, the training loss is the Charbonnier loss. For the rest IR task, the L1 loss is commonly used during the training. 4) For IR in AWC, we adopted similar training settings as Transweather [84], the model is trained for a total of 750K iterations.

#### 1.3. Data and Evaluation

The training dataset and test datasets for different IR tasks are described in this section. For IR in AWC, we used a similar training pipeline as Transweather with only one phase.

Additionally, for tasks such as image super-resolution (SR), JPEG CAR, image denoising, and demosaicking, how the corresponding low-quality images are generated is also briefly introduced below.

**Image SR.** For image SR, the LR image is synthesized by Matlab bicubic downsampling function before the training. We investigated the upscaling factors  $\times 2$ ,  $\times 3$ , and  $\times 4$ .

- The training datasets: DIV2K [3] and Flickr2K [53].
- The test datasets: Set5 [7], Set14 [94], BSD100 [63], Urban100 [30], and Manga109 [64].

**Image Denoising.** For image denoising, we conduct experiments on both color and grayscale image denoising. During training and testing, noisy images are generated by adding independent additive white Gaussian noise (AWGN) to the original images. The noise levels are set to  $\sigma = 15, 25, 50$ . We train individual networks at different noise levels. The network takes the noisy images as input and tries to predict noise-free images. Additionally, we also tried to train one model for all noise levels.

- The training datasets: DIV2K [3], Flickr2K [53], WED [60], and BSD400 [63].
- The test datasets for color image: CBS68 [63], Kodak24 [24], McMaster [102], and Urban100 [30].
- The test datasets for grayscale image: Set12 [97], BSD68 [63], and Urban100 [30].

**JPEG compression artifact removal.** For JPEG compression artifact removal, the JPEG image is compressed by the cv2 JPEG compression function. The compression function is characterized by the quality factor. We investigated four compression quality factors including 10, 20, 30, and 40. The smaller the quality factor, the more the image is compressed, meaning a lower quality. We also trained one model to deal with different quality factors.

- The training datasets: DIV2K [3], Flickr2K [53], and WED [60].
- The test datasets: Classic5 [23], LIVE1 [75], Urban100 [30], BSD500 [5].

**IR in Adverse Weather Conditions.** For IR in adverse weather conditions, the model is trained on a combination of images degraded by a variety of adverse weather conditions. The same training and test dataset is used as in Transweather [84]. The training data comprises 9,000 images sampled from Snow100K [56], 1,069 images from Raindrop [71], and 9,000 images from Outdoor-Rain [44]. Snow100K includes synthetic images degraded by snow, Raindrop consists of real raindrop images, and Outdoor-Rain contains synthetic images degraded by both fog and

Table A. The details of the *Fractal-IR* stages and *Fractal-IR* layers per stage for both architectures.

	U-shaped architecture			Columnar architecture	
	Down Stages	Upstages	Latent Stage	<i>Fractal-IR</i> -Base	<i>Fractal-IR</i> -Large
Num. of <i>Fractal-IR</i> Stages	3	3	1	6	8
Num. of <i>Fractal-IR</i> Layer/Stage	6	6	6	6	8

Table B. Space and time complexity of classical attention mechanisms.

Attn. method	Time complexity	Space complexity	Max receptive field of two transformer layers
Global Attn.	$\mathcal{O}((4 + 2\gamma)BHW C^2 + 2B(HW)^2 C)$	$\mathcal{O}(4BHW C + B(HW)^2 h)$	$H \times W$
Window Attn. ( $p \times p$ )	$\mathcal{O}((4 + 2\gamma)BHW C^2 + 2BHW p^2 C)$	$\mathcal{O}(4BHW C + BHW h p^2)$	$2p \times 2p$
Window Attn. ( $8P \times 8P$ )	$\mathcal{O}((4 + 2\gamma)BHW C^2 + 128BHW p^2 s^2 C)$	$\mathcal{O}(4BHW C + 64BHW h p^2 s^2)$	$16P \times 16P$
The proposed	$\mathcal{O}((5 + 2\gamma)BHW C^2 + \frac{3}{2}BHW(p^2 + s^2)C)$	$\mathcal{O}(3BHW C + BHW h \max(p^2, s^2))$	$16P \times 16P$

rain streaks. The proposed method is tested on both synthetic and real-world datasets.

- The test datasets: test1 dataset [44, 45], the RainDrop test dataset [71], and the Snow100k-L test.

**Image Deblurring.** For single-image motion deblurring,

- The training datasets: GoPro [66] dataset.
- The test datasets: GoPro [66], HIDE [76], RealBlur-R [73], and RealBlur-J [73] datasets.

**Defocus Deblurring.** The task contains two modes including single-image defocus deblurring and dual-pixel defocus deblurring. For single-image defocus deblurring, only the blurred central-view image is available. For dual-pixel defocus deblurring, both the blurred left-view and right-view images are available. The dual-pixel images could provide additional information for defocus deblurring and thus could lead to better results. PSNR, SSIM, and mean absolute error (MAE) on the RGB channels are reported. Additionally, the image perceptual quality score LPIPS is also reported.

- The training datasets: DPDD [1] training dataset. The training subset contains 350 scenes.
- The test datasets: DPDD [1] test dataset. The test set contains 37 indoor scenes and 39 outdoor scenes

**Image Demosaicking.** For image demosaicking, the mosaic image is generated by applying a Bayer filter on the ground-truth image. Then the network try to restore high-quality image. The mosaic image is first processed by the default `Matlab` demosaic function and then passed to the network as input.

- The training datasets: DIV2K [3] and Flickr2K [53].
- The test datasets: Kodak [24], McMaster [102].

## 2. Space and Time Complexity

We compare the space and time complexity and the effective receptive field of the proposed method with a couple of other self-attention methods including global attention and window attention. Suppose the input feature has the dimension  $B \times C \times H \times W$ , the window size of window attention is  $p$ , the number of attention heads is  $h$ , larger patch size

of the proposed L2 information flow is  $P = s \times p$ , the expansion ratio of the MLP in transformer layer is  $\gamma$ . For time complexity, both self-attention and the feed-forward network are considered. For space complexity, we consider the tensors that have to appear in the memory at the same time, which include the input tensor, the query tensor, the key tensor, the value tensor, and the attention map.

The time complexity of the proposed transformer layer is

$$\mathcal{O} \left( (5 + 2\gamma)BHW C^2 + \frac{3}{2}BHW p^2 C + \frac{3}{2}BHW s^2 C + 9\gamma BHW C \right). \quad (9)$$

The last term is very small compared with the former two terms and can be omitted. Thus, the time complexity is simplified as

$$\mathcal{O} \left( (5 + 2\gamma)BHW C^2 + \frac{3}{2}BHW p^2 C + \frac{3}{2}BHW s^2 C \right). \quad (10)$$

The space complexity of the proposed transformer layer is

$$\mathcal{O}(3BHW C + BHW h \max(p^2, s^2)). \quad (11)$$

The maximum receptive field of two consecutive transformer layers is  $16P$ .

In Tab. B, we list the space and time complexity, and maximum receptive field of global attention, window attention, and the proposed method. As shown in this table, window attention is much more efficient than global attention but with the cost of reduced receptive field. The proposed fractal information flow mechanism is more efficient than window attention in propagating information to the global range. As shown in the third row, to achieve the same receptive field as the proposed method, the space and time complexity of window attention is much higher than that of the proposed method.

## 3. Model Scaling-up

As mentioned in the main paper, when the initially designed SR model is scaled up from about 10M parameters

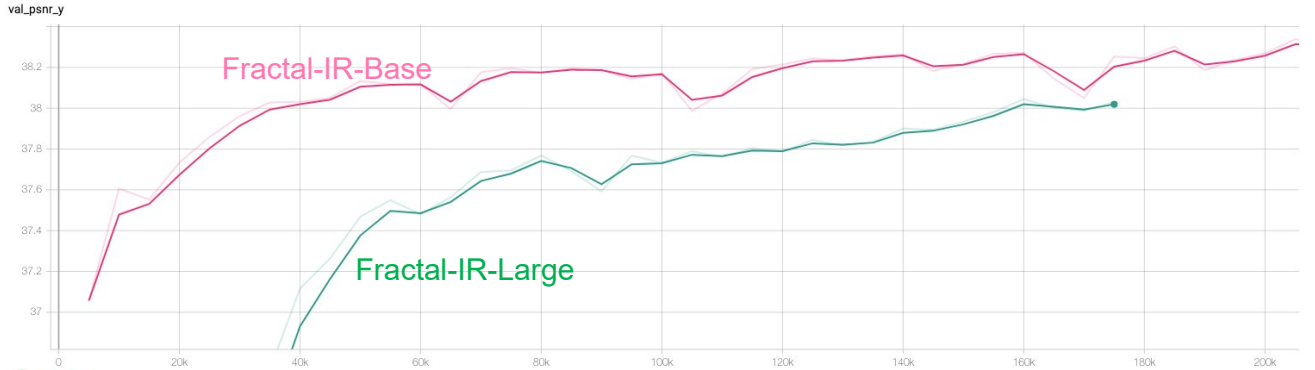


Figure B. When the SR model is scale-up from *Fractal-IR-B* to *Fractal-IR-L*, the model *Fractal-IR-L* converges slower than *Fractal-IR-B*.

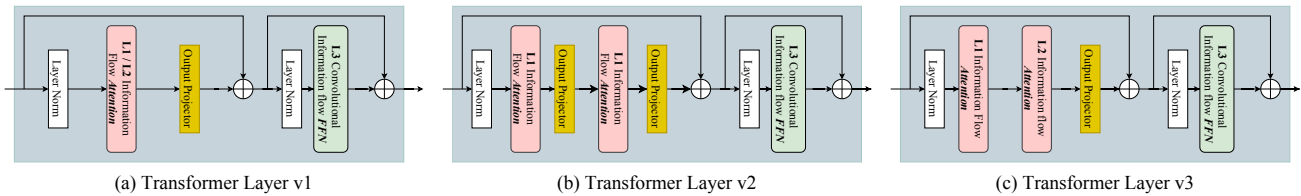


Figure C. Comparison of three types of transformer layers designed in this paper.

Table C. Model scaling-up exploration with SR.

Scale	Model Size	Warm up	Conv Type	PSNR				
				Set5	Set14	BSD100	Urban100	Manga109
2x	15.69	No	conv1	38.52	34.47	32.56	34.17	39.77
2x	57.60	No	conv1	38.33	34.17	32.46	33.60	39.37
2x	57.60	Yes	conv1	38.41	34.33	32.50	33.80	39.51
2x	54.23	Yes	linear	<b>38.56</b>	<b>34.59</b>	<b>32.58</b>	<b>34.32</b>	<b>39.87</b>
2x	55.73	Yes	conv3	<b>38.65</b>	<b>34.48</b>	<b>32.58</b>	<b>34.33</b>	<b>40.12</b>
3x	15.87	No	conv1	35.06	30.91	29.48	30.02	34.41
3x	57.78	No	conv1	34.70	30.62	29.33	29.11	33.96
3x	57.78	Yes	conv1	34.91	30.77	29.39	29.53	34.12
3x	54.41	Yes	linear	<b>35.13</b>	<b>31.04</b>	<b>29.52</b>	<b>30.20</b>	<b>34.54</b>
3x	55.91	Yes	conv3	<b>35.14</b>	<b>31.03</b>	<b>29.51</b>	<b>30.22</b>	<b>34.76</b>
4x	15.84	No	conv1	33.00	29.11	27.94	27.67	31.41
4x	57.74	No	conv1	33.08	29.19	27.97	27.83	31.56
4x	57.74	Yes	conv1	32.67	28.93	27.83	27.11	30.97
4x	54.37	Yes	linear	<b>33.06</b>	<b>29.16</b>	<b>27.99</b>	<b>27.93</b>	<b>31.66</b>
4x	55.88	Yes	conv3	<b>33.06</b>	<b>29.16</b>	<b>27.97</b>	<b>27.87</b>	<b>31.54</b>

to about 50M parameters, the performance of the large SR model becomes worse. The effect is shown in Fig. B. The PSNR curve on the Set5 dataset for the first 200k iterations is shown in this figure. The scale-up model *Fractal-IR-L* converges slower than the smaller model *Fractal-IR-B*. The same phenomenon could be observed by comparing the first two rows for each upscaling factor in Tab. C, where scaled-up models converge to worse local minima. A similar problem occurs in previous works [11, 53].

#### 4. Ablation study

As mentioned in the main paper, to investigate the effect of  $\mathcal{L}_1$  and  $\mathcal{L}_2$  information flow, we designed three versions of the *Fractal-IR* layers. The architecture of the three trans-

former layers is shown in Fig. C.

## 5. More Quantitative Experimental Results

Due to the limited space in the main manuscript, we only report a part of the experimental result. In this section, we show the full quantitative experimental results for each IR task in the following.

### 5.1. Single-image defocus deblurring

In addition to the dual-pixel defocus deblurring results, we also shown single-image defocus deblurring results in Tab. G

**One model for multiple degradation levels.** For image denoising and JPEG CAR, we trained a single model to handle multiple degradation levels. This setup makes it possible to apply one model to deal with images that have been degraded under different conditions, making the model more flexible and generalizable. During training, the noise level is randomly sampled from the range [15, 75] while the JPEG compression quality factor is randomly sampled from the range [10, 90]. The degraded images are generated online. During the test phase, the degradation level is fixed to a certain value. The experimental results are summarized in Fig. 6 of our main manuscript. The numerical results for grayscale JPEG CAR are presented in Tab. 12 of our main manuscript. These results show that in the one-model-multiple-degradation setting †, the proposed *Fractal-IR* achieves the best performance.

Table D. *Classical image SR* results. Top-2 results are highlighted in red and blue.

Method	Scale	Params [M]	Set5		Set14		BSD100		Urban100		Manga109	
			PSNR $\uparrow$	SSIM $\uparrow$	PSNR $\uparrow$	SSIM $\uparrow$	PSNR $\uparrow$	SSIM $\uparrow$	PSNR $\uparrow$	SSIM $\uparrow$	PSNR $\uparrow$	SSIM $\uparrow$
EDSR [53]	2 $\times$	40.73	38.11	0.9602	33.92	0.9195	32.32	0.9013	32.93	0.9351	39.10	0.9773
SRFBN [50]	2 $\times$	2.14	38.11	0.9609	33.82	0.9196	32.29	0.9010	32.62	0.9328	39.08	0.9779
RCAN [103]	2 $\times$	15.44	38.27	0.9614	34.12	0.9216	32.41	0.9027	33.34	0.9384	39.44	0.9786
SAN [18]	2 $\times$	15.71	38.31	0.9620	34.07	0.9213	32.42	0.9028	33.10	0.9370	39.32	0.9792
HAN [67]	2 $\times$	63.61	38.27	0.9614	34.16	0.9217	32.41	0.9027	33.35	0.9385	39.46	0.9785
NLSA [65]	2 $\times$	42.63	38.34	0.9618	34.08	0.9231	32.43	0.9027	33.42	0.9394	39.59	0.9789
IPT [9]	2 $\times$	115.48	38.37	-	34.43	-	32.48	-	33.76	-	-	-
SwinIR [52]	2 $\times$	11.75	38.42	0.9623	34.46	0.9250	32.53	0.9041	33.81	0.9427	39.92	0.9797
CAT-A [13]	2 $\times$	16.46	38.51	0.9626	34.78	0.9265	32.59	0.9047	34.26	0.9440	40.10	0.9805
ART [95]	2 $\times$	16.40	38.56	0.9629	34.59	0.9267	32.58	0.9048	34.3	0.9452	40.24	0.9808
EDT [47]	2 $\times$	11.48	38.63	0.9632	34.80	0.9273	32.62	0.9052	34.27	0.9456	40.37	0.9811
GRL-B [48]	2 $\times$	20.05	38.67	0.9647	35.08	0.9303	32.67	0.9087	35.06	0.9505	40.67	0.9818
HAT [11]	2 $\times$	20.62	38.73	0.9637	35.13	0.9282	32.69	0.9060	34.81	0.9489	40.71	0.9819
Fractal-IR-B (Ours)	2 $\times$	14.68	38.71	0.9657	35.16	0.9299	32.73	0.9087	34.94	0.9484	40.81	0.9830
HAT-L [11]	2 $\times$	40.70	38.91	0.9646	35.29	0.9293	32.74	0.9066	35.09	0.9505	41.01	0.9831
Fractal-IR-L (Ours)	2 $\times$	39.07	38.87	0.9663	35.27	0.9311	32.77	0.9092	35.16	0.9505	41.22	0.9846
EDSR [53]	3 $\times$	43.68	34.65	0.9280	30.52	0.8462	29.25	0.8093	28.80	0.8653	34.17	0.9476
SRFBN [50]	3 $\times$	2.83	34.70	0.9292	30.51	0.8461	29.24	0.8084	28.73	0.8641	34.18	0.9481
RCAN [103]	3 $\times$	15.63	34.74	0.9299	30.65	0.8482	29.32	0.8111	29.09	0.8702	34.44	0.9499
SAN [18]	3 $\times$	15.90	34.75	0.9300	30.59	0.8476	29.33	0.8112	28.93	0.8671	34.30	0.9494
HAN [67]	3 $\times$	64.35	34.75	0.9299	30.67	0.8483	29.32	0.8110	29.10	0.8705	34.48	0.9500
NLSA [65]	3 $\times$	45.58	34.85	0.9306	30.70	0.8485	29.34	0.8117	29.25	0.8726	34.57	0.9508
IPT [9]	3 $\times$	115.67	34.81	-	30.85	-	29.38	-	29.49	-	-	-
SwinIR [52]	3 $\times$	11.94	34.97	0.9318	30.93	0.8534	29.46	0.8145	29.75	0.8826	35.12	0.9537
CAT-A [13]	3 $\times$	16.64	35.06	0.9326	31.04	0.8538	29.52	0.8160	30.12	0.8862	35.38	0.9546
ART [95]	3 $\times$	16.58	35.07	0.9325	31.02	0.8541	29.51	0.8159	30.1	0.8871	35.39	0.9548
EDT [47]	3 $\times$	11.66	35.13	0.9328	31.09	0.8553	29.53	0.8165	30.07	0.8863	35.47	0.9550
GRL-B [48]	3 $\times$	20.24	35.12	0.9353	31.27	0.8611	29.56	0.8235	30.92	0.8990	35.76	0.9566
HAT [11]	3 $\times$	20.81	35.16	0.9335	31.33	0.8576	29.59	0.8177	30.7	0.8949	35.84	0.9567
Fractal-IR-B (Ours)	3 $\times$	14.87	35.11	0.9372	31.37	0.8598	29.60	0.8240	30.79	0.8977	35.92	0.9583
HAT-L [11]	3 $\times$	40.88	35.28	0.9345	31.47	0.8584	29.63	0.8191	30.92	0.8981	36.02	0.9576
Fractal-IR-L (Ours)	3 $\times$	39.26	35.20	0.9380	31.55	0.8616	29.67	0.8256	31.07	0.9020	36.12	0.9588
EDSR [53]	4 $\times$	43.09	32.46	0.8968	28.80	0.7876	27.71	0.7420	26.64	0.8033	31.02	0.9148
SRFBN [50]	4 $\times$	3.63	32.47	0.8983	28.81	0.7868	27.72	0.7409	26.60	0.8015	31.15	0.9160
RCAN [103]	4 $\times$	15.59	32.63	0.9002	28.87	0.7889	27.77	0.7436	26.82	0.8087	31.22	0.9173
SAN [18]	4 $\times$	15.86	32.64	0.9003	28.92	0.7888	27.78	0.7436	26.79	0.8068	31.18	0.9169
HAN [67]	4 $\times$	64.20	32.64	0.9002	28.90	0.7890	27.80	0.7442	26.85	0.8094	31.42	0.9177
NLSA [65]	4 $\times$	44.99	32.59	0.9000	28.87	0.7891	27.78	0.7444	26.96	0.8109	31.27	0.9184
IPT [9]	4 $\times$	115.63	32.64	-	29.01	-	27.82	-	27.26	-	-	-
SwinIR [52]	4 $\times$	11.90	32.92	0.9044	29.09	0.7950	27.92	0.7489	27.45	0.8254	32.03	0.9260
CAT-A [13]	4 $\times$	16.60	33.08	0.9052	29.18	0.7960	27.99	0.7510	27.89	0.8339	32.39	0.9285
ART [95]	4 $\times$	16.55	33.04	0.9051	29.16	0.7958	27.97	0.7510	27.77	0.8321	32.31	0.9283
EDT [47]	4 $\times$	11.63	33.06	0.9055	29.23	0.7971	27.99	0.7510	27.75	0.8317	32.39	0.9283
GRL-B [48]	4 $\times$	20.20	33.10	0.9094	29.37	0.8058	28.01	0.7611	28.53	0.8504	32.77	0.9325
HAT [11]	4 $\times$	20.77	33.18	0.9073	29.38	0.8001	28.05	0.7534	28.37	0.8447	32.87	0.9319
Fractal-IR-B (Ours)	4 $\times$	14.83	33.14	0.9095	29.40	0.8029	28.08	0.7611	28.44	0.8448	32.90	0.9323
HAT-L [11]	4 $\times$	40.85	33.30	0.9083	29.47	0.8015	28.09	0.7551	28.60	0.8498	33.09	0.9335
Fractal-IR-L (Ours)	4 $\times$	39.22	33.22	0.9103	29.49	0.8041	28.13	0.7622	28.72	0.8514	33.13	0.9366

## 5.2. Generalizing one model to more types degradations

To validate the generalization capability of the proposed method to different types of degradation, we conducted the following experiments. First, we used the same model for both denoising and JPEG compression artifact removal tasks. Notably, a single model was trained to handle varying levels of degradation. The experimental results for denoising are shown in Tab. H while the results for JPEG compression artifact removal are shown in Tab. E and Tab. 12 of our main manuscript. Second, we performed experiments on image restoration under adverse weather conditions, including rain, fog, and snow. The results are shown in Tab. 14 of our main manuscript. These three sets of experiments collectively highlight that the proposed fractal information

flow mechanism enables training a single model that generalizes effectively to various types and levels of degradation.

## 6. Comparison with ShuffleFormer and Shuffle Transformer

We compare with Random shuffle transformer (ShuffleFormer) [89] and Shuffle transformer [31]. Both methods use spatial shuffle operations to facilitate non-local information exchange, with one being random and the other deterministic.

Random Shuffle Transformer (ShuffleFormer) [89] applies random shuffling on the spatial dimension, which increases the probability of global information existing within a local window. While this operation extends the receptive field globally in a single step, it compromises the relevance



Table E. *Color image JPEG compression artifact removal results.*

Set	QF	JPEG		†QGAC		†FBCNN		†DRUNet		†Fractal-IR (Ours)		SwinIR		GRL-S		Fractal-IR (Ours)	
		PSNR	SSIM	PSNR	SSIM	PSNR	SSIM	PSNR	SSIM	PSNR	SSIM	PSNR	SSIM	PSNR	SSIM	PSNR	SSIM
LIVEI	10	25.69	0.7430	27.62	0.8040	27.77	0.8030	<b>27.47</b>	<b>0.8045</b>	<b>28.24</b>	<b>0.8149</b>	28.06	0.8129	<b>28.13</b>	<b>0.8139</b>	<b>28.36</b>	<b>0.8180</b>
	20	28.06	0.8260	29.88	0.8680	30.11	0.8680	<b>30.29</b>	<b>0.8743</b>	<b>30.59</b>	<b>0.8786</b>	30.44	0.8768	<b>30.49</b>	<b>0.8776</b>	<b>30.66</b>	<b>0.8797</b>
	30	29.37	0.8610	31.17	0.8960	31.43	0.8970	<b>31.64</b>	<b>0.9020</b>	<b>31.95</b>	<b>0.9055</b>	31.81	0.9040	<b>31.85</b>	<b>0.9045</b>	<b>32.02</b>	<b>0.9063</b>
	40	30.28	0.8820	32.05	0.9120	32.34	0.9130	<b>32.56</b>	<b>0.9174</b>	<b>32.88</b>	<b>0.9205</b>	32.75	0.9193	<b>32.79</b>	<b>0.9195</b>	<b>32.94</b>	<b>0.9210</b>
BSD500	10	25.84	0.7410	27.74	<b>0.8020</b>	<b>27.85</b>	0.7990	27.62	0.8001	<b>28.26</b>	<b>0.8070</b>	28.22	0.8075	<b>28.26</b>	<b>0.8083</b>	<b>28.35</b>	<b>0.8092</b>
	20	28.21	0.8270	30.01	0.8690	30.14	0.8670	<b>30.39</b>	<b>0.8711</b>	<b>30.58</b>	<b>0.8741</b>	30.54	0.8739	<b>30.57</b>	<b>0.8746</b>	<b>30.61</b>	<b>0.8740</b>
	30	29.57	0.8650	31.330	0.8980	31.45	0.8970	<b>31.73</b>	<b>0.9003</b>	<b>31.93</b>	<b>0.9029</b>	31.90	0.9025	<b>31.92</b>	<b>0.9030</b>	<b>31.99</b>	<b>0.9035</b>
	40	30.52	0.8870	32.25	0.9150	32.36	0.9130	<b>32.66</b>	<b>0.9168</b>	<b>32.87</b>	<b>0.9193</b>	32.84	0.9189	<b>32.86</b>	<b>0.9192</b>	<b>32.92</b>	<b>0.9195</b>
Urban100	10	24.46	0.7612	-	-	-	-	<b>27.10</b>	<b>0.8400</b>	<b>28.78</b>	<b>0.8666</b>	28.18	0.8586	<b>28.54</b>	<b>0.8635</b>	<b>29.11</b>	<b>0.8727</b>
	20	26.63	0.8310	-	-	-	-	<b>30.17</b>	<b>0.8991</b>	<b>31.12</b>	<b>0.9087</b>	30.53	0.9030	<b>30.93</b>	<b>0.9067</b>	<b>31.36</b>	<b>0.9115</b>
	30	27.96	0.8640	-	-	-	-	<b>31.49</b>	<b>0.9189</b>	<b>32.42</b>	<b>0.9265</b>	31.87	0.9219	<b>32.24</b>	<b>0.9247</b>	<b>32.57</b>	<b>0.9279</b>
	40	28.93	0.8825	-	-	-	-	<b>32.36</b>	<b>0.9301</b>	<b>33.26</b>	<b>0.9363</b>	32.75	0.9329	<b>33.09</b>	<b>0.9348</b>	<b>33.37</b>	<b>0.9373</b>

Table F. *Single image motion deblurring on RealBlur dataset.* †: Methods trained on RealBlur.

Method	RealBlur-R	RealBlur-J	Average
	PSNR↑ / SSIM↑	PSNR↑ / SSIM↑	PSNR↑ / SSIM↑
†DeblurGAN-v2	36.44 / 0.935	29.69 / 0.870	33.07 / 0.903
†SRN [80]	38.65 / 0.965	31.38 / 0.909	35.02 / 0.937
†MPRNet [92]	39.31 / 0.972	31.76 / 0.922	35.54 / 0.947
†MIMO-UNet+ [14]	- / -	32.05 / 0.921	- / -
†MAXIM-3S [83]	39.45 / 0.962	<b>32.84 / 0.935</b>	36.15 / 0.949
†BANet [82]	39.55 / 0.971	32.00 / 0.923	35.78 / 0.947
†MSSNet [36]	39.76 / 0.972	32.10 / 0.928	35.93 / 0.950
DeepRFT+ [62]	39.84 / 0.972	32.19 / 0.931	36.02 / 0.952
†Stripformer [81]	<b>39.84 / 0.974</b>	32.48 / 0.929	36.16 / 0.952
†GRL-B [48]	<b>40.20 / 0.974</b>	32.82 / 0.932	<b>36.51 / 0.953</b>
†Fractal-IR-L (Ours)	<b>40.40 / 0.976</b>	<b>32.92 / 0.933</b>	<b>36.66 / 0.954</b>

of pixels within the window. In contrast, the fractal information flow proposed in this paper progressively propagates information from local to global while preserving the relevance of attended pixels. A comparison with ShuffleFormer on image deblurring is presented in Tab. 9 of our main manuscript. *Fractal-IR* outperforms ShuffleFormer by a significant margin while using 55.5% fewer parameters. This demonstrates the effectiveness of the fractal information flow method introduced in this work.

Shuffle Transformer [31] employs a spatial shuffle operation to aggregate information from distant pixels or tokens. However, it differs from the proposed *Fractal-IR* in several key aspects. First, Shuffle Transformer does not enable progressive information propagation within a fractal tree structure. Second, its shuffle operation is based on a fixed grid size of  $g = 8$ . The distance between pixels in the shuffled window is  $H/g$  and  $W/g$  along the two axes, which directly depends on the image size. For large images (e.g., 1024 pixels), this design forces distant pixels to attend to one another, often introducing irrelevant information. Consequently, this operation is unsuitable for image restoration tasks, where image sizes can become extremely large. In contrast, the L2 information flow attention proposed in this paper limits the maximum patch size, thereby constraining the maximum distance between pixels at this stage. This re-

striction enhances the relevance of pixel interactions, making it more effective for image restoration tasks.

## 7. More Visual Results

To further support the effectiveness and generalizability of the proposed *Fractal-IR* intuitively. We provide more visual comparison in terms of image SR (Fig. D, ), JPEG compression artifact removal (Fig. F ), image restoration in adverse weather conditions (Fig. H) blow. As shown in those figures, the visual results of the proposed *Fractal-IR* are improved compared with the other methods.

## 8. Limitations

Despite the state-of-the-art performance of *Fractal-IR*, our explorations towards scaling up the model for IR in this paper are still incomplete. Scaling up the IR model is intricate, involving considerations like model design, data collection, and computing resources. We hope our work can catalyze positive impacts on future research, encouraging more comprehensive scaling-up explorations and propelling IR into the domain of large-scale models.

## 9. Impact Statement

The proposed *Fractal-IR* framework significantly advances image restoration by addressing critical challenges in model scalability, efficiency, and generalization across diverse degradation types and resolutions. By leveraging a fractal-based design, *Fractal-IR* effectively balances local and global information processing, reducing the computational overhead typically associated with self-attention mechanisms in transformers. Furthermore, our holistic approach to model scaling ensures that *Fractal-IR* can be trained effectively at larger capacities, enabling it to capture richer image patterns and deliver state-of-the-art performance across a broad range of restoration tasks. This work opens up new possibilities for deploying scalable, efficient, and generalizable models in real-world image restoration.

Table G. *Defocus deblurring* results. **S**: single-image defocus deblurring. **D**: dual-pixel defocus deblurring.

Method	Indoor Scenes				Outdoor Scenes				Combined			
	PSNR $\uparrow$	SSIM $\uparrow$	MAE $\downarrow$	LPIPS $\downarrow$	PSNR $\uparrow$	SSIM $\uparrow$	MAE $\downarrow$	LPIPS $\downarrow$	PSNR $\uparrow$	SSIM $\uparrow$	MAE $\downarrow$	LPIPS $\downarrow$
EBDB <sub>S</sub> [34]	25.77	0.772	0.040	0.297	21.25	0.599	0.058	0.373	23.45	0.683	0.049	0.336
DMENet <sub>S</sub> [41]	25.50	0.788	0.038	0.298	21.43	0.644	0.063	0.397	23.41	0.714	0.051	0.349
JNB <sub>S</sub> [77]	26.73	0.828	0.031	0.273	21.10	0.608	0.064	0.355	23.84	0.715	0.048	0.315
DPDNet <sub>S</sub> [1]	26.54	0.816	0.031	0.239	22.25	0.682	0.056	0.313	24.34	0.747	0.044	0.277
KPAC <sub>S</sub> [79]	27.97	0.852	0.026	0.182	22.62	0.701	0.053	0.269	25.22	0.774	0.040	0.227
IFAN <sub>S</sub> [42]	28.11	0.861	0.026	0.179	22.76	0.720	0.052	0.254	25.37	0.789	0.039	0.217
Restormer <sub>S</sub> [93]	<b>28.87</b>	<b>0.882</b>	<b>0.025</b>	<b>0.145</b>	<b>23.24</b>	<b>0.743</b>	<b>0.050</b>	<b>0.209</b>	<b>25.98</b>	<b>0.811</b>	<b>0.038</b>	<b>0.178</b>
Fractal-IR <sub>S</sub> -B (Ours)	<b>28.73</b>	<b>0.885</b>	<b>0.025</b>	<b>0.140</b>	<b>23.66</b>	<b>0.766</b>	<b>0.048</b>	<b>0.196</b>	<b>26.13</b>	<b>0.824</b>	<b>0.037</b>	<b>0.169</b>
DPDNet <sub>D</sub> [1]	27.48	0.849	0.029	0.189	22.90	0.726	0.052	0.255	25.13	0.786	0.041	0.223
RDPD <sub>D</sub> [2]	28.10	0.843	0.027	0.210	22.82	0.704	0.053	0.298	25.39	0.772	0.040	0.255
Uformer <sub>D</sub> [88]	28.23	0.860	0.026	0.199	23.10	0.728	0.051	0.285	25.65	0.795	0.039	0.243
IFAN <sub>D</sub> [42]	28.66	0.868	<b>0.025</b>	0.172	23.46	0.743	0.049	0.240	25.99	0.804	0.037	0.207
Restormer <sub>D</sub> [93]	<b>29.48</b>	<b>0.895</b>	<b>0.023</b>	<b>0.134</b>	<b>23.97</b>	<b>0.773</b>	<b>0.047</b>	<b>0.175</b>	<b>26.66</b>	<b>0.833</b>	<b>0.035</b>	<b>0.155</b>
Fractal-IR <sub>D</sub> -B (Ours)	<b>29.70</b>	<b>0.902</b>	<b>0.023</b>	<b>0.116</b>	<b>24.46</b>	<b>0.798</b>	<b>0.045</b>	<b>0.154</b>	<b>27.01</b>	<b>0.848</b>	<b>0.034</b>	<b>0.135</b>

Table H. *Color and grayscale image denoising* results. A single model is trained to handle multiple noise levels.

Method	Params [M]	Color								Grayscale						
		CBSD68			Kodak24			McMaster		Urban100		Set12		Urban100		
		$\sigma=15$	$\sigma=25$	$\sigma=50$	$\sigma=15$	$\sigma=25$	$\sigma=50$	$\sigma=15$	$\sigma=25$	$\sigma=50$	$\sigma=15$	$\sigma=25$	$\sigma=50$	$\sigma=15$	$\sigma=25$	$\sigma=50$
DnCNN [35]	0.56	33.90	31.24	27.95	34.60	32.14	28.95	33.45	31.52	28.62	32.98	30.81	27.59	32.67	30.35	27.18
FFDNet [99]	0.49	33.87	31.21	27.96	34.63	32.13	28.98	34.66	32.35	29.18	33.83	31.40	28.05	32.75	30.43	27.32
IRCNN [98]	0.19	33.86	31.16	27.86	34.69	32.18	28.93	34.58	32.18	28.91	33.78	31.20	27.70	32.76	30.37	27.12
DRUNet [100]	32.64	34.30	31.69	28.51	35.31	32.89	29.86	35.40	33.14	30.08	34.81	32.60	29.61	33.25	30.94	27.90
Restormer [93]	26.13	<b>34.39</b>	<b>31.78</b>	<b>28.59</b>	<b>35.44</b>	<b>33.02</b>	<b>30.00</b>	<b>35.55</b>	<b>33.31</b>	<b>30.29</b>	<b>35.06</b>	<b>32.91</b>	<b>30.02</b>	<b>33.35</b>	<b>31.04</b>	<b>28.01</b>
Fractal-IR (Ours)	22.33	<b>34.43</b>	<b>31.80</b>	<b>28.60</b>	<b>35.42</b>	<b>33.00</b>	<b>29.95</b>	<b>35.67</b>	<b>33.43</b>	<b>30.38</b>	<b>35.46</b>	<b>33.32</b>	<b>30.47</b>	<b>33.49</b>	<b>31.18</b>	<b>28.14</b>

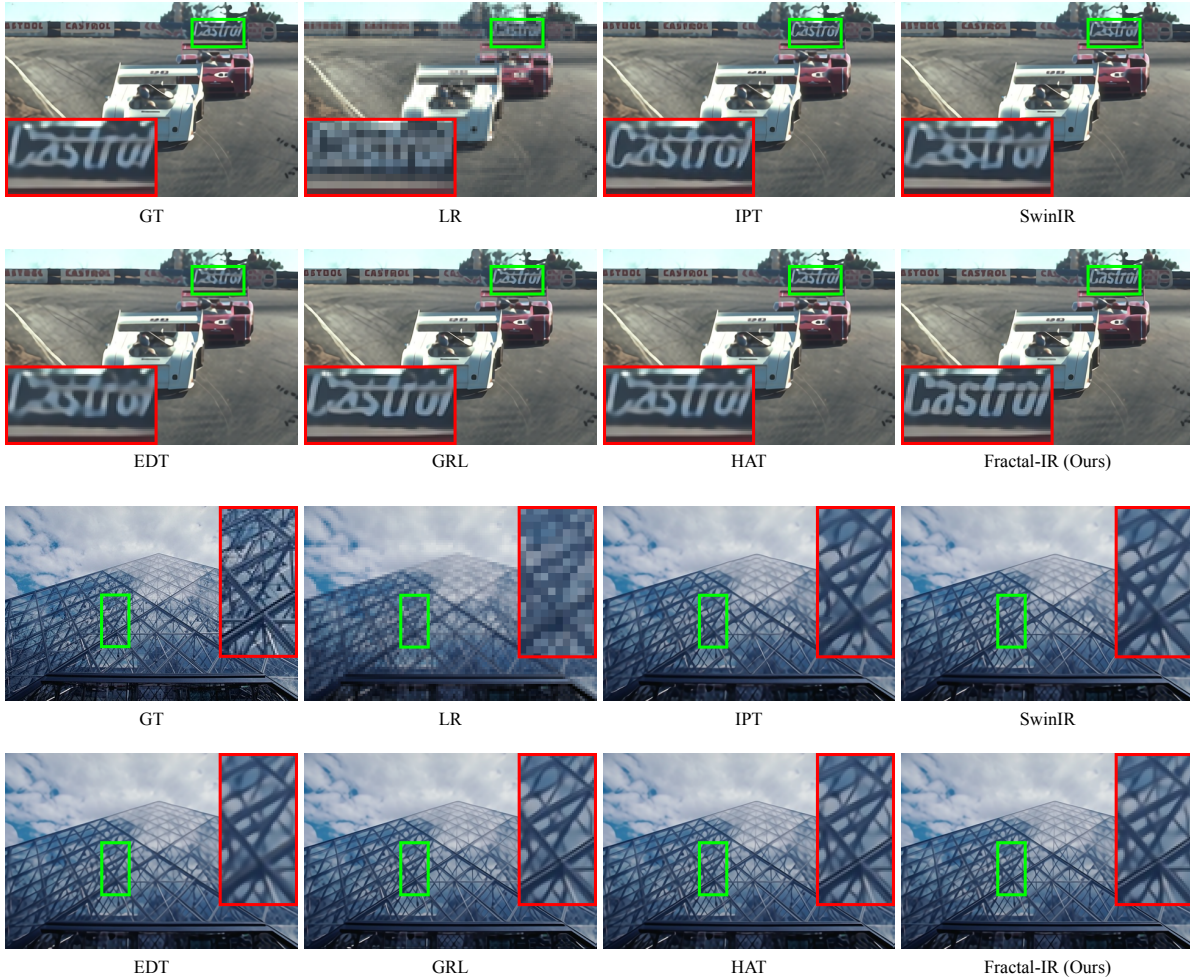


Figure D. Visual results for classical image  $\times 4$  SR on B100 dataset.

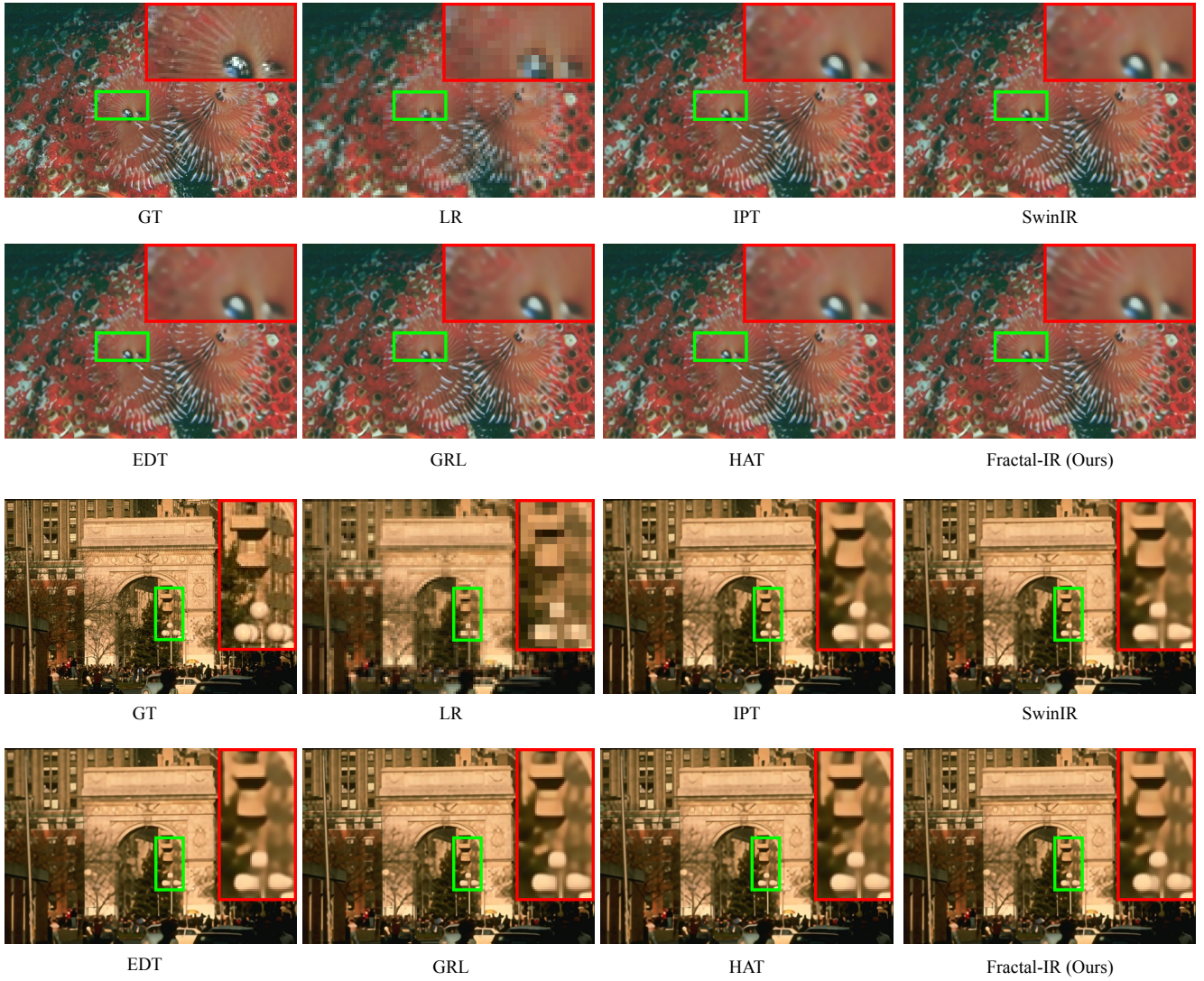


Figure E. Visual results for classical image SR on B100 dataset. The upscaling factor is  $\times 4$ .



Figure F. Visual results for color image JPEG compression artifact removal on BSD500 dataset. The quality factor of JPEG image compression is 10.



Figure G. Visual results for color image JPEG compression artifact removal on LIVE1 dataset. The quality factor of JPEG image compression is 10.



Figure H. Visual results for restoring images in adverse weather conditions.